Structural and functional analysis of the C-terminal region of FliG, an essential motor component of *Vibrio* Na^+-driven flagella

Yohei Miyanoiri[2,#,*], Atsushi Hijikata[3,#], Yuuki Nishino[1,#], Mizuki Gohara[1], Yasuhiro Onoue[1], Seiji Kojima[1], Chojiro Kojima[4], Tsuyoshi Shirai[3], Masatsune Kainosho[2] and Michio Homma[1,*]

[1]Division of Biological Science, and [2]Structural Biology Research Center, Graduate School of Science, Nagoya University, Chikusa-ku, Nagoya, 464-8602

[3]Department of Bioscience, Nagahama Institute of Bio-Science and Technology, 1266 Tamura, Nagahama, 526-0829

[4] Graduate School of Engineering, Division of Material Science and Engineering, Yokohama National University, Hodogaya-ku, Yokohama, 240-8501

Running title:

Structural and functional analysis of FliG

[#]**These authors contributed equally**

***Correspondence to Michio Homma (Lead Contact) and Yohei Miyanoiri:**

g44416a@cc.nagoya-u.ac.jp (MH) or miyanoiri.youhei@h.mbox.nagoya-u.ac.jp (YM).

Keywords: NMR; FliG; rotor; flagellar motor

Abbreviations: PomA, Polar flagellar motility protein A; PomB, Polar flagellar motility protein B; SDS-PAGE, sodium dodecyl sulfate-polyacrylamide gel electrophoresis; NMR, Nuclear magnetic resonance

SUMMARY

The flagellar motor protein complex, which consists of rotor and stator proteins. Their interaction generates torque of flagellum which rotates bi-directionally, clockwise (CW) and counter-clockwise (CCW). FliG, one of the rotor proteins, consists of three domains: N-terminal ($FliG_N$), middle ($FliG_M$) and C-terminal ($FliG_C$). We have identified point mutations in $FliG_C$ from *Vibrio alginolyticus,* which affect the flagellar motility. To understand the molecular mechanisms, we explored the structural and dynamic properties of $FliG_C$ from both wild type and motility defective mutants. From NMR analysis, changes in signal intensities and chemical shifts between wild type and the CW-biased mutant $FliG_C$ are observed in Cα1-6 domain. Molecular dynamic simulations indicated the conformational dynamics of $FliG_C$ at sub-microsecond timescale, but not in the CW-biased mutant. Accordingly, we infer that the dynamic properties of atomic interactions around helix α1 in the Cα1-6 domain of $FliG_C$ contribute to ensure the precise regulation of the motor switching.

INTRODUCTION

The bacterial flagellum is comprised of filament, hook, and basal body. The basal body contains multiple ring-like structures, such as L, P, MS, and C ring. The rotation of bacterial flagellar motor is bi-directional. The motor can rotate in both clockwise (CW) and counter-clockwise (CCW) directions. Rotor, the rotating part of bacterial flagellar motor, is comprised of MS and C rings. The

MS ring is embedded in the inner membrane and made up of FliF protein. The C ring is located under the MS ring and consists of three proteins: FliG, FliM, and FliN (Macnab, 2003;Terashima et al., 2008). The complex of these components is involved in the switching between CW and CCW rotations of the flagellar motor. Owing to the rotational switching ability, the complex is also called the "switch complex." The switching is regulated by the chemotaxis signaling pathway (Sourjik and Armitage, 2010); FliM is the component involved in this pathway. When FliM binds to the phosphorylated CheY, which is a chemotactic regulator, CCW rotation is suppressed, so that the motor rotates CW. When CheY is not phosphorylated, it cannot bind FliM and the flagellar motor rotates in the CCW direction. FliG, another component in the switch complex, is involved directly in the rotation. FliG contains three domains: N terminal domain ($FliG_N$), middle domain ($FliG_M$), and C terminal domain ($FliG_C$) (Figure 1A). The third component of the switch complex, FliN, is thought to have a role in the flagellar export. Stator, the non-rotating part of the motor, is anchored to the peptidoglycan layer and interacts with the rotor to generate torque. Stator assembles around the rotor depending on H^+ (for example, *Escherichia coli*) or Na^+ (for example, *Vibrio*) influx in the stator. These ion influxes induce conformational change in the stator protein. The stator components are named MotA and MotB in the H^+-driven motor of *E. coli* or PomA and PomB in the Na^+-driven motor of *Vibrio alginolyticus* (Li et al., 2011). MotB and PomB have a single transmembrane region and a peptidoglycan-binding region. MotA and PomA have four transmembrane regions and one large loop in the cytoplasm. It

80 is thought that the interaction between the large loop of the MotA/PomA subunit
81 and the rotor component, FliG, generates the torque (Takekawa et al., 2014).
82 The charged residues in this large cytoplasmic loop of the stator MotA/PomA
83 subunit and the charged residues in the C terminal domain of $FliG_C$ are proposed
84 to be the sites of interaction between the two proteins. We have shown that
85 $FliG_C$ of *Vibrio* is functional in *E. coli* and can interact with MotA of *E. coli* to
86 generate torque (Yorimitsu et al., 2003; Yakushi et al., 2006).
87 Extensive mutational analysis of FliG from *E. coli* and *Salmonella*,
88 identified a large number of mutations that affect the flagellation (*fla*), the
89 rotational bias (*che*) and the torque generation (*mot*) (Irikura et al., 1993; Lloyd
90 et al., 1996). In *E. coli*, a mutation in FliG neutralizes the effect of a mutation in
91 MotB, which conferred non-motility phenotype (Van Way et al., 2004). In
92 *Salmonella*, a deletion in $helix_{MC}$, which bridges $FliG_M$ and $FliG_C$, influenced
93 the rotational bias (CW-locked) (Togashi et al., 1997; Minamino et al., 2011).
94 The structures of FliG from various species, with different truncations and
95 mutations, have been determined by X-ray crystallography. Crystal structure of
96 the complex using fragments of *Thermotoga maritima* revealed the interaction
97 between FliG and FliM (Paul et al., 2011; Vartanian et al., 2012). Structural
98 analyses demonstrated that the packing of $helix_{MC}$ affects the orientation of
99 $FliG_M$ and $FliG_{C,}$ causing conformational changes in the rotor ring, which in turn
100 leads to the switch in the rotation (Lee et al., 2010; Baker et al., 2016). Although
101 a very large number of mutational or structural studies have been conducted, the

molecular mechanism as to how the mutations in FliG affect the torque generation or rotational switching of flagellar motor remain largely unknown.

We generated various mutants of FliG from *Vibrio alginolyticus* (*Va*), which affected the motility and flagellation (Kojima et al., 2011; Onoue et al., 2015; Nishikino et al., 2016). Some of them, which have single amino acid substitution in *Va* $FliG_C$, resulted in a critical defect in flagellar rotation. In the present study, we purified the wild type and mutant fragments of *Va* $FliG_C$ (Figure 1) and analyzed their structural and functional characteristics. Using a combination of NMR and molecular dynamics (MD) simulations of the fragments of *Va* $FliG_C$, we explored the differences in the structural properties between the wild type and motility-defective mutants at atomic resolution. The results suggest that change in the conformation of *Va* $FliG_C$ contributes to the generation of torque and flagellar bi-directional switching.

RESULTS AND DISCUSSION

Structural properties of *Va* $FliG_C$

On the basis of the crystal structure of FliG middle and C-terminal domains in *T. maritima* (PDB: 1lkv), we built a homology model of *Va* $FliG_C$, which consists of two domains. The first domain, C1 consist of an Armadillo repeat motif, ARM_C (G214 to L252) comprised of 3 helices, involved in the interaction with FliM (Brown *et al.*, 2007; Grunenfelder *et al.*, 2003; Passmore *et al.*, 2008; Paul

et al., 2011). The second domain, C2 (M253 to L351), contains the MFXF (M253 to F256) motif and six tightly packed helices (Cα1-6, F256 – D337) (Brown *et al.*, 2002; Lee *et al.*, 2010; Minamino *et al.*, 2011) (Figure 1B). It was reported that the immotile phenotype was given by the mutations in the α1, α2 and α3 of C2 in *Salmonella* (Irikura et al., 1993) To analyze the structural properties of *Va* $FliG_C$ in solution, we prepared uniformly ^{13}C, ^{15}N-labeled His-*Va* $FliG_C$ [(U-^{13}C,^{15}N) His-*Va* $FliG_C$] and performed NMR analysis. Although His-*Va* $FliG_C$ showed well-separated amide signals in ^{1}H-^{15}N HSQC spectrum (Figure 2A, Figure S1), the amide signals in G214 to V260 were relatively broader and could not be assigned completely. It appears that His-*Va* $FliG_C$ has several conformations.

To elucidate the correlation between the structural properties and motor function of *Va* $FliG_C$, we measured the ^{1}H-^{15}N HSQC spectrum of His-*Va* $FliG_C$ containing single amino acid substitutions, which resulted in defective motility. Previously, we made the FliG mutations L259Q, L270R, and L271P which completely abolished the motility of *Vibrio* cells and the A282T mutation which conferred CW-biased phenotype (Kojima *et al.*, 2011). The mutations had been introduced according to the mutations of the conserved residues which conferred the *mot* phenotype in *Salmonella* (Irikura et al., 1993). These amino acid residues located in the Cα1-6 in $FliG_C$ and are well conserved in several species. According to the model structure of *Va* $FliG_C$, these four residues form the hydrophobic core of the Cα1-6 domain. The uniformly ^{15}N-labeled His-*Va* $FliG_C$(L270R) and His-*Va* $FliG_C$(L271P) mutants showed only few signals that

were broader than the wild type signals (Figures 2B, C). NMR samples of these mutant proteins precipitated out partially after 2–3-hour experiments at 288K. Although the L259Q mutant [His-*Va* $FliG_C$(L259Q)] emitted highly sensitive amide signals in ^{1}H-^{15}N HSQC spectrum (Figure 2D), the number of observed signals was smaller than that of the wild type and the mutant protein degraded within few hours at 288K. On the other hand, the CW-biased mutant [His-*Va* $FliG_C$(A282T)] was relatively stable for 2-3 days and emitted separated amide signals in the ^{1}H-^{15}N HSQC (Figure 2E) spectrum. These results indicate that the loss or weaken hydrophobic interaction by the mutations except A282T in the domain decreased the protein stability resulting in the defect of bacterial motility.

The thermal stability of wild type *Va* $FliG_C$ and the mutated protein with L259Q, L270R, and L271P mutations has been measured by differential scanning calorimetry and three of them have more trypsin susceptibility than the wild type (Gohara *et al.*, 2014). Similar protease susceptibility by mutations of $FliG_C$ had been reported in *E. coli* and it was supposed that there was the relation between the protease sensitivity and the Mot^- phenotype (Lloyd and Blair, 1997). The specific denaturation enthalpy change (ΔH) of the L271P mutant differed the most and was one-fifth of that of the wild type $FliG_C$. In the ^{1}H-^{15}N HSQC spectrum of His-*Va* $FliG_C$(L259Q), most of the amide signals were observed in the range of 8.0–8.5 ppm in ^{1}H axis, and these signal intensities were relatively stronger than those observed in other regions (Figure 2D). This is a typical spectrum pattern of the unstructured regions of proteins.

Therefore, it is likely that the structure of His-*Va* $FliG_C$(L259Q) is partially unfolded. The number of observed amide signals in the ^{1}H-^{15}N HSQC spectra of His-*Va* $FliG_C$(L270R) and His-*Va* $FliG_C$(L271P) was significantly smaller than that expected from the primary amino acid sequence. Moreover, these observed signals were much broader than those of the wild type (Figure 2). As mentioned above, these two mutant proteins easily precipitated out. Thus, we think that the L270R and L271P mutations induce a structural disruption resulting in aggregation. The residues L270 or L271 and L259 belong to the α2 and α1 helix, respectively. These hydrophobic residues are highly conserved in several species. $FliG_C$ structures indicate that these helices interact with other helices. Therefore, these Leu residues may play a crucial role in forming the hydrophobic core structure and maintaining the appropriate structure of $FliG_C$.

Structural dynamics of Cα1-6 of *Va* $FliG_C$ and its CW-biased mutant

To elucidate the structural and dynamic properties of the Cα1-6 of *Va* $FliG_C$ and *Va* $FliG_C$(A282T), we constructed a new $FliG_C$ fragment (His-*Va* $FliG_{C2}$, Figure 1A) and expressed [U-^{13}C,^{15}N] His-*Va* $FliG_{C2}$ fragments of wild type and its A282T mutant in *E. coli.* Expression level of His-*Va* $FliG_{C2}$ was much higher than that of His-*Va* $FliG_C$. The purified protein did not precipitate or degrade within 2 weeks at 288K. Therefore, all backbone (^{1}HN, ^{15}NH, $^{13}C\alpha$, $^{13}C\beta$, ^{13}CO) signals could be assigned unambiguously by the conventional triple resonance NMR experiments (Figure 3; Table S1). From chemical shift-based secondary structure analysis using TALOS-N (Shen and Bax, 2015), six helices,

194 [α1(F256-V260), α2(D264-R272), α3(Q276-L283), α4(D288-K296),
195 α5(K300-E311) and α6(V318-D337)], were identified in His-*Va* $FliG_{C2}$ (Table
196 S1). Remarkably, the amide signals in N terminal region (M253 to V260) of
197 His-*Va* $FliG_{C2}$, which could not be observed in His-*Va* $FliG_{C}$, were clearly
198 observed and could be assigned.
199 We also carried out NMR measurements on His-*Va* $FliG_{C2}$(A282T).
200 Although some amide signals showed large changes in chemical shift compared
201 to those of His-*Va* $FliG_{C2}$, the backbone NMR signals were assigned clearly,
202 except for the region from M253 to V260, which corresponds to the MFXF
203 motif and α1 of His-*Va* $FliG_{C2}$ (Table S2). In the ^{1}H-^{15}N HSQC spectrum of
204 His-*Va* $FliG_{C2,}$ some broadened signals were observed and could not be assigned
205 owing to the low sensitivity.
206 Next, we compared the ^{1}H-^{15}N HSQC spectra of His-*Va* $FliG_{C2}$ and
207 His-*Va* $FliG_{C2}$(A282T). Large chemical shift perturbation (> 0.1 ppm) and signal
208 broadening were observed in the mutant and were mapped onto *Va* $FliG_{C}$ model
209 structure (Figures 3 and 4). Interestingly, these signal changes were observed
210 not only around the A282T region (α3-α4), but also in the MFXF motif, α1, α5,
211 and α6 regions, which are relatively farther in the amino acid sequence from the
212 A282T mutation site. These results indicated that some intra molecular
213 interactions present in His-*Va* $FliG_{C2}$ are partially disrupted by the A282T
214 mutation. We also measured T_2 value of amide ^{15}N for His-*Va* $FliG_{C2}$ and
215 His-*Va* $FliG_{C2}$(A282T). The ^{15}N T_2 of α3-α4 region in His-*Va* $FliG_{C2}$ was longer
216 than that of A282T mutant (Figure S2). We suggest that a slow (milli to micro

second scale) conformational exchange occurs in the α3-α4 region in His-*Va* $FliG_{C2}$(A282T).

To understand the molecular basis of the conformational differences between the wild type and CW-biased mutant proteins at atomic resolution, molecular dynamics simulations were performed for the wild type (*Va* $FliG_C$) and mutant [*Va* $FliG_C$(A282T)] proteins. From the trajectory analysis of the simulation, the ARM_C domain of *Va* $FliG_C$ showed a larger root mean square deviation (RMSD) on average during the simulation (3.1 Å ±0.8 for WT, 4.1 Å ±1.0 for A282T, respectively) as compared with that of the Cα1-6 domain (1.8 Å ±0.4 for WT, 1.5 Å ±0.3 for A282T, respectively), indicating that the ARM_C domain is intrinsically flexible and assumes multiple conformations as observed in the NMR analysis. We, therefore, focused on the structural difference of the Cα1-6 domains between *Va* $FliG_C$ and *Va* $FliG_C$(A282T). For *Va* $FliG_C$, the values of the RMSD of the trajectories from the initial structure showed a bimodal distribution with peaks at 1.3 Å and 2.0 Å, whereas that of *Va* $FliG_C$(A282T) showed a single peak at 1.4 Å. The degree of retention of the native secondary structure of *Va* $FliG_C$(A282T) during the simulation was comparable to that of *Va* $FliG_C$, rather it seemed to be slightly higher than that of *Va* $FliG_C$ in α1 and α3 helices (Figure S3).

Cluster analysis of the backbone structures of Cα1-6 domain of *Va* $FliG_C$ in the trajectories revealed that there were at least three representative conformations (S1, S2 and S3) (Figures 5A, B). In contrast, a single conformation was dominant in *Va* $FliG_C$(A282T) (Figure 5C, D). These results

indicated that, the structure of *Va* $FliG_C$(A282T) was restricted into one of the three conformations of *Va* $FliG_C$, at submicrosecond timescale. We then compared the 3D structures of the representative conformations with the initial structure as the reference. The RMSD of the backbone atoms in each conformation of the Cα1-6 domain of *Va* $FliG_C$ were 1.3 Å (WT S1), 1.9 Å (WT S2), and 1.9 Å (WT S3). Although the overall structure of the representative conformations was kept around the initial structure, especially for the α6 region, a large structural deviation was observed in the loop region between the helices α5 and α6. The representative conformation of the *Va* $FliG_C$(A282T) was also compared with the reference structure, and its RMSD value was 1.3 Å, comparable to that of the wild type. The WT S2 conformation differed the most from that of the others. The differences in the regions of α1, α2, and α4 contributed most to the structural differences. The backbone RMSDs of the conformation in the Cα1-6 domain of *Va* $FliG_C$(A282T) relative to that in the wild type were 1.8 Å (WT S1), 2.5 Å (WT S2), and 1.7 Å (WT S3). Hence, the overall conformation of *Va* $FliG_C$ (A282T) was relatively close to that of S3. The deviation of the loop region was as large as that of the wild type conformation, but the other regions, with the exception of α1, had smaller deviations than those in the wild type.

The amino acid residue of position 282 were buried and formed a part of the hydrophobic core in the Ca1-6 domain of both *Va* $FliG_C$ and *Va* $FliG_C$ (A282T). In *Va* $FliG_C$(A282T), there was an additional hydrogen bond between the hydroxyl group of T282 side chain and the carbonyl group of V278

backbone, which was retained during the simulation (Figure 6). The hydrogen bond formation between the T282 and the backbone on α4 in the hydrophobic environment would be attributed to the gain of the thermodynamic stability in the Cα1-6 domain of *Va* $FliG_C$(A282T). Furthermore, F256 in α1(also the second Phe in the MFXF motif), another residues forming the hydrophobic core of the Cα1-6 domain, was in contact with the Cβ atom of A282. In the structure of *Va* $FliG_C$(A282T), the substitution of A282 with Thr, which introduced a methyl group at the γ-position, precludes the interaction between the Cβ atom at the position and the side chain atoms of F256, thus, distancing α1 from α3 and α4. When the angle (θ) and distance (d) between helices α1 and α4 were measured for each trajectory of *Va* $FliG_C$ and *Va* $FliG_C$(A282T) (Figure 6), *Va* $FliG_C$ showed two peaks at 20° - 9.5 Å and 40° -10.4 Å, whereas *Va* $FliG_C$(A282T) showed a single peak at 35° - 11.1 Å. Since θ was well correlated with d, the helix rearrangement between α1 and α4 seemed to be an important factor for the conformational change observed in *Va* $FliG_C$. The difference in the helix rearrangement between the *Va* $FliG_C$ and *Va* $FliG_C$(A282T) would be attributed to the local conformation alteration around α1 helix through a steric repulsion between T282 and F256. Simultaneously, the additional hydrogen bond between T282 side chain hydroxyl group and the V278 backbone carbonyl group adds to the thermodynamic stability in the Cα1-6 domain of *Va* $FliG_C$(A282T). The results of the computational simulation could explain the experimental observation of the slow state exchange in α3–α4 (Figure S3) and large chemical shift around the α1 (Figure 4).

These structural effects caused by a single amino acid substitution would restrict the conformational variety in the Cα1-6 domain, which was not the case with the wild type. The helix rearrangement around α1, as observed in the wild type, seemed to be coupled to the motion of the N-terminal region of *Va* $FliG_C$, which presumably play an important role in switching the directions of the flagellar rotation.

Role of $FliG_C$ in the rotational switching

The amide signals in the ^{1}H-^{15}N HSQC spectrum of the A282T mutant with CW-biased phenotype were widely separated and the signal intensities were homogeneous (Figures 2E, 3B). The A282T mutant did not precipitate or degrade after NMR experiments. Therefore, the A282T mutation, unlike the other mutations, did not appear to disrupt the protein fold. Comparison of the ^{1}H-^{15}N HSQC spectra of His-*Va* $FliG_{C2}$ and His-*Va* $FliG_{C2}$(A282T) showed that structural rearrangement occurred in Cα1-6 domain, especially in the MFXF motif, α1, α3 to α4, α5, and α6 (Figure 4). In addition, structural fluctuations in milli to micro-second timescale were specifically observed in α3 to α4 region of A282T (Figure S2). This dynamic property in α3 and α4 helices resulting from the A282T mutation seemed to be caused by an additional hydrogen bond formation, as estimated by molecular dynamics simulation (Figure 6). Molecular dynamics simulation also suggested changes in structural dynamics of α1 to α4 helices (Figures 5 and 6).

From the ^{1}H-^{15}N HSQC spectrum of His-*Va* FliG$_{C}$, amide signals of the ARM$_{C}$-MFXF-α1 region, G214-V260, were broadened and could not be assigned completely. The molecular dynamics simulations also suggested flexibilities in this region. On the other hand, as mentioned above, amide signals of MFXF-α1 region are clearly observed in the ^{1}H-^{15}N HSQC spectrum of His-*Va* FliG$_{C2}$, which are truncated in the ARM$_{C}$ domain. These NMR and molecular dynamics simulation analyses suggested that the MFXF-α1 helix of His-*Va* FliG$_{C}$ acts as a hinge between ARM$_{C}$ and Cα1-6 domains of *Va* FliG$_{C}$, which interact with each other. These multiple interactions may produce several transient structures of *Va* FliG$_{C}$ in solution state. This is consistent with the α helical content estimated by CD spectra (Gohara *et al.*, 2014). This α helical content in His-*Va* FliG$_{C}$ was smaller than that estimated by secondary structure prediction. In contrast, the α helical content of His-*Va* FliC$_{C2}$, as estimated by CD spectra, was almost the same as that estimated by secondary structure prediction. Other species also exhibit these phenomena. Two distinct conformations of FliG$_{C}$ were observed in the crystal structure of FliG from *Helicobacter pylori* (Lam *et al.*, 2012). In the ^{1}H-^{15}N HSQC spectrum of *T. maritima* FliG$_{C}$ also, the amide signals of ARM$_{C}$-MFXF-α1 helix region (G196-L242) were broadened and could not be assigned completely (Dyer *et al.*, 2009).

The molecular dynamics simulation results in this study suggested three representative conformations for the wild type *Va* FliG$_{C}$, but only one conformation for *Va* FliG$_{C}$(A282T). It means that the additional methyl group at

331 the A282 site because of the substitution with threonine partially disrupts the
332 hydrophobic interactions between MFXF-α1(F256) and α3 (T282). The
333 distribution of the multiple interactions between ARM_C and Cα1-6 may result in
334 a single conformation. As a result, bi-directional (CW and CCW) flagellar motor
335 function might have been abolished in the A282T mutant.
336 Crystal structures of $FliG_C$ domains indicate several conformations
337 between the ARM_C and Cα1-6 domains connected by the MFXF motif (Brown
338 *et al.*, 2002; Lee *et al.*, 2010; Minamino *et al.*, 2011). The structural analyses of
339 $FliG_{MC}$ demonstrate that the orientation of $FliG_C$ is prompted by the rotational
340 freedom of the MFXF motif (Lee *et al.*, 2010; Lam *et al.*, 2012). By comparing
341 the six known crystal structures of $FliG_C$ from various species, we found that the
342 rearrangement patterns of ARM_C-Cα1-6 could be largely divided into two
343 groups: one containing the structure of CW-locked mutant, and the other one
344 containing the putative "CCW-conformation" of *A. aeolicus* FliG (Figure S4).
345 To illustrate the difference in the domain orientation between the two groups,
346 we used two structural parameters: the dihedral angle of hinge residue F254 (in
347 *V. alginolyticus*) (Lam *et al.*, 2012), and the orientation of helix α0 (the last
348 helix in the ARM_C domain) relative to Cα1-6 domain. We then plotted the two
349 parameter values (ϕ of F254 and the angle between the α0 and α6 helices) for
350 the structures of MD trajectories of *Va* $FliG_C$ and *Va* $FliG_C$(A282T). The
351 parameter values for *Va* $FliG_C$ were clustered mainly in two regions,
352 corresponding to those of the crystal structures in each group, whereas, for *Va*
353 $FliG_C$ (A282T), the values were in a single region, corresponding to that for the

CW-locked mutant (Figure 7). It is noteworthy that the MD simulation of *Va* $FliG_C$ was started from the homology-based model structure based on the $FliG_C$ of *T. maritima* (PDB code: 1lkv), in which the orientation of ARM_C- Cα1-6 domains was close to that of the CW-locked mutant. This was in good agreement with results of the recent molecular simulation study of conformer ensembles, by showing a bimodal distribution of the rotation angle of the torque helix, relative to the MFVF hinge (Pandini *et al.*, 2016). The authors of this study also showed that the CW-locked mutant (PDB code: 3ajc) displayed an asymmetric distribution of the angle between the torque helix and the hinge.

The actual CW and CCW conformations of FliG should be determined in the context of the flagellar motor protein complex with the other components forming the ring-shape structure. Nevertheless, considering the correlation between the single conformational state of the Cα1-6 domain of $FliG_C$ observed in the MD simulations and the CW-biased phenotype of A282T, we hypothesized that the major conformation observed in the simulations for *Va* $FliG_C$(A282T) was the CW-conformation. In our simulation, the A282T mutation would have a repulsive effect on the interaction between F256 on MFXF-α1 and T282 on α3 resulting in the fixation of the α1-α3 orientation, which was not observed in *Va* $FliG_C$. Consequently, it would restrict the movements of the MFXF hinge of ARM_C-Cα1-6 domain and α0 helix and lock the structure in the CW-conformation. The NMR measurements were highly supportive of the computational hypothesis. Although further investigations are needed to validate our hypothesis in greater detail, to the best of our knowledge,

this is the first report that describes at atomic resolution, the molecular mechanism by which a point mutation in FliG affects the rotational switching.

STAR★METHODS

Detailed methods are provided in the online version of this paper and included the following:

- ● **KEY RESOURCES TABLE**
- ● **CONTACT FOR REAGENT AND RESOURCES SHARING**
- ● **EXPERIMENTAL MODEL AND SUBJECT DETAILS**
  - ○ Strains Used in Protein Production
- ● **METHOD DETAILS**
  - ○ Protein expression in *E. coli* and purification
  - ○ NMR Spectroscopy
  - ○ Secondary structure analysis
  - ○ Homology modeling
  - ○ Molecular dynamics simulation
- ● **QUANTIFICATION AND STATISTICAL ANALYSIS**

● DATA AND SOFTWARE AVAILABILITY

○ Data Resources

ACCESSION NUMBERS

The identification accession numbers of the chemical shift data in the BioMagResBank (BMRB; http://www.bmrb.wisc.edu) are as follows. His-*Va* $FliG_{C2}$ (BMRB accession number: 12010), His-*Va* $FliG_{C2}$(A282T) (BMRB accession number: 12011).

SUPPLEMENTAL INFORMATION

Document S1. Figures S1-S3 and Tables S1 and S2

AUTHOR CONTRIBUTIONS

Conceptualization: Y.M., A.H. and M.H.; Methodology, Y.O., S.K., Y.N., and M.G.; Investigation: Y.M., A.H. and Y.N.; Writing – Original Draft: Y.M., A.H., and Y.N.; NMR Data/Discussion: Y.M., Y.N., M.G., C.K., and M.K.; Structure modeling/Discussion: A.H., Y.O. and T.S., Writing – Review & Editing: M.H., Y.M., and A.H.; Funding Acquisition, Resources, and Supervision: M.H., S.K, A.H., T.S., and Y.M.

ACKNOWLEDGEMENTS

This research was supported by Grants-in-aid for scientific research from the Ministry of Education, Science and Culture of Japan (24117004 and 23247024 to MH, or 24657087 to SK), the Platform for Drug Design, Informatics, and Structural Lifescience (PDIS) (16am0101042j0005) from the AMED to AH and TS, and Program for leading Graduate Schools of Japan, Science for the Promotion of Science to MG. YM was supported by JSPS KAKENHI Grants-in-Aid for Young Scientists (B) (23770111 and 25840021) and a Grant-in-Aid for Scientific Research (C) (15K06966).

Conflict of interest

None declared.

References

Baker, M. A., Hynson, R. M., Ganuelas, L. A., Mohammadi, N. S., Liew, C. W., Rey, A. A., Duff, A. P., Whitten, A. E., Jeffries, C. M., Delalez, N. J., Morimoto, Y. V., Stock, D., Armitage, J. P., Turberfield, A. J., Namba, K., Berry, R. M. and Lee, L. K. (2016). Domain-swap polymerization drives the self-assembly of the bacterial flagellar motor. Nat. Struct. Mol. Biol. *23*, 197-203.

Brown, P. N., Hill, C. P. and Blair, D. F. (2002). Crystal structure of the middle and C-terminal domains of the flagellar rotor protein FliG. EMBO J. *21*, 3225-3234.

Brown, P. N., Terrazas, M., Paul, K. and Blair, D. F. (2007). Mutational analysis of the flagellar protein FliG: sites of interaction with FliM and implications for organization of the switch complex. J. Bacteriol. *189*, 305-312.

Delaglio, F., Grzesiek, S., Vuister, G. W., Zhu, G., Pfeifer, J. and Bax, A. (1995) NMRPipe: a multidimensional spectral processing system based on UNIX pipes. J. Biomol. NMR *6*, 277-293.

Dyer, C. M., Vartanian, A. S., Zhou, H. and Dahlquist, F. W. (2009). A molecular mechanism of bacterial flagellar motor switching. J. Mol. Biol. *388*, 71-84.

Gohara, M., Kobayashi, S., Abe-Yoshizumi, R., Nonoyama, N., Kojima, S., Asami, Y. and Homma, M. (2014). Biophysical characterization of the C-terminal region of FliG, an essential rotor component of the Na^+-driven flagellar motor. J. Biochem. *155*, 83-89.

Grunenfelder, B., Gehrig, S. and Jenal, U. (2003). Role of the cytoplasmic C terminus of the FliF motor protein in flagellar assembly and rotation. J. Bacteriol. *185*, 1624-1633.

Hijikata, A., Yura, K., Noguti, T. and Go, M. (2011). Revisiting gap locations inamino acid sequence alignments and a proposal for a method to improve them by introducing solvent accessibility. Proteins *79*, 1868-1877.

Irikura, V. M., Kihara, M., Yamaguchi, S., Sockett, H. and Macnab, R. M. (1993) *Salmonella typhimurium fliG* and *fliN* mutations causing defects in assembly, rotation, and switching of the flagellar motor. J. Bacteriol. 175, 802-810.

Kojima, S., Nonoyama, N., Takekawa, N., Fukuoka, H. and Homma, M. (2011). Mutations targeting the C-terminal domain of FliG can disrupt motor assembly in the Na^+-driven flagella of *Vibrio alginolyticus*. J. Mol. Biol. *414*, 62-74.

Lam, K. H., Ip, W. S., Lam, Y. W., Chan, S. O., Ling, T. K. and Au, S. W. (2012). Multiple conformations of the FliG C-terminal domain provide insight into flagellar motor switching. Structure *20*, 315-325.

476 Lee, L. K., Ginsburg, M. A., Crovace, C., Donohoe, M. and Stock, D. (2010).
477 Structure of the torque ring of the flagellar motor and the molecular basis
478 for rotational switching. Nature *466*, 996-1000.
479 Li, N., Kojima, S. and Homma, M. (2011). Sodium-driven motor of the polar
480 flagellum in marine bacteria *Vibrio*. Genes Cells *16*, 985-999.
481 Lloyd, S. A. and Blair, D. F. (1997) Charged residues of the rotor protein FliG
482 essential for torque generation in the flagellar motor of *Escherichia coli*. J.
483 Mol. Biol. *266*, 733-744.
484 Lloyd, S. A., Tang, H., Wang, X., Billings, S. and Blair, D. F. (1996) Torque
485 generation in the flagellar motor of Escherichia coli: evidence of a direct
486 role for FliG but not for FliM or FliN. J. Bacteriol. *178*, 223-231.
487 Macnab, R. (1995). Flagellar switch, In J.A. Hoch and T.J. Silhavey (ed),
488 Two-component signal transduction. American Society for Microbiology,
489 Washington, D.C., p.181-199.
490 Macnab, R. M. (2003). How bacteria assemble flagella. Annu. Rev. Microbiol.
491 *57*, 77-100.
492 Marti-Renom, M. A., Stuart, A. C., Fiser, A., Sanchez, R., Melo, F. and Sali, A.
493 (2000). Comparative protein structure modeling of genes and genomes.
494 Annu. Rev. Biophys. Biomol. Struct. *29*, 291-325.
495 Minamino, T., Imada, K., Kinoshita, M., Nakamura, S., Morimoto, Y. V. and
496 Namba, K. (2011). Structural insight into the rotational switching
497 mechanism of the bacterial flagellar motor. PLoS Biol. *9*, e1000616.
498 Nishikino, T., Zhu, S., Takekawa, N., Kojima, S., Onoue, Y. and Homma, M.
499 (2016). Serine suppresses the motor function of a periplasmic PomB
500 mutation in the *Vibrio* flagella stator. Genes Cells *21*, 505-516.
501 Onoue, Y., Kojima, S. and Homma, M. (2015). Effect of FliG three amino acids
502 deletion in Vibrio polar-flagellar rotation and formation. J. Biochem. *158*,
503 523-529.
504 Pandini, A., Morcos, F. and Khan, S. (2016). The Gearbox of the bacterial
505 flagellar motor switch. Structure *24*, 1209-1220.
506 Passmore, S. E., Meas, R. and Marykwas, D. L. (2008). Analysis of the
507 FliM/FliG motor protein interaction by two-hybrid mutation suppression
508 analysis. Microbiology *154*, 714-724.

509 Paul, K., Brunstetter, D., Titen, S. and Blair, D. F. (2011). A molecular
510 mechanism of direction switching in the flagellar motor of Escherichia
511 coli. Proc. Natl. Acad. Sci. USA *108*, 17171-17176.
512 Pronk, S., Pall, S., Schulz, R., Larsson, P., Bjelkmar, P., Apostolov, R., Shirts,
513 M. R., Smith, J. C., Kasson, P. M., van der Spoel, D., Hess, B. and
514 Lindahl, E. (2013). GROMACS 4.5: a high-throughput and highly
515 parallel open source molecular simulation toolkit. Bioinformatics *29*,
516 845-854.
517 Shen, Y. and Bax, A. (2015). Protein structural information derived from NMR
518 chemical shift with the neural network program TALOS-N. Methods Mol.
519 Biol. 1260, 17-32.
520 Sourjik, V. and Armitage, J. P. (2010). Spatial organization in bacterial
521 chemotaxis. EMBO J. *29*, 2724-2733.
522 Takekawa, N., Kojima, S. and Homma, M. (2014). Contribution of Many
523 Charged residues at the stator-rotor interface of the Na^+-driven flagellar
524 motor to torque generation in *Vibrio alginolyticus*. J. Bacteriol. *196*,
525 1377-1385.
526 Terashima, H., Kojima, S. and Homma, M. (2008). Flagellar motility in bacteria
527 structure and function of flagellar motor. Int. Rev. Cell Mol. Biol. *270*,
528 39-85.
529 Togashi, F., Yamaguchi, S., Kihara, M., Aizawa, S. I. and Macnab, R. M.
530 (1997). An extreme clockwise switch bias mutation in *fliG* of S*almonella*
531 *typhimurium* and its suppression by slow-motile mutations in *motA* and
532 *motB*. J. Bacteriol. *179*, 2994-3003.
533 Van Way, S. M., Millas, S. G., Lee, A. H. and Manson, M. D. (2004). Rusty,
534 jammed, and well-oiled hinges: Mutations affecting the interdomain
535 region of FliG, a rotor element of the *Escherichia coli* flagellar motor. J.
536 Bacteriol. *186*, 3173-3181.
537 Vartanian, A. S., Paz, A., Fortgang, E. A., Abramson, J. and Dahlquist, F. W.
538 (2012) Structure of flagellar motor proteins in complex allows for insights
539 into motor structure and switching. J. Biol. Chem. *287*, 35779-35783.
540 Yakushi, T., Yang, J., Fukuoka, H., Homma, M. and Blair, D. F. (2006). Roles
541 of charged residues of rotor and stator in flagellar rotation: comparative

study using H^+-driven and Na^+-driven motors in *Escherichia coli*. J. Bacteriol. *188*, 1466-1472.

Yorimitsu, T., Mimaki, A., Yakushi, T. and Homma, M. (2003). The conserved charged residues of the C-terminal region of FliG, a rotor component of the Na^+-driven flagellar motor. J. Mol. Biol. *334*, 567-583.

Figure legends

Figure 1. Structure of the FliG protein

(A) Schematic representation showing the organization of full-length *Vibrio alginolyticus* (*Va*) FliG and His-tagged *Va* $FliG_C$ proteins used in this study. The *Va* FliG consists of three domains, N-terminal domain ($FliG_N$, blue), Middle domain ($FliG_M$, green) and C terminal domain ($FliG_C$, red). $FliG_C$ is comprised of two globular helical domains, C1 (G214-L252, pink) and C2 (M253-L351, cyan and orange). The C1 consists of Armadillo repeat motif, ARM_C. The MFXF motif (M253-F256, cyan) and tightly packed 6 helices, Cα1-6 (F256-D337, orange) are belongs to C2. The 6x His-Tag is shown as yellow. (B) The model structure of *Va* $FliG_C$. The ARM_C, MFXF and Cα1-6 is colored pink, cyan and orange, respectively. Side chains of the residues involved in the motor function in *Va* $FliG_C$ are shown in green.

Figure 2. NMR analysis for His-*Va* $FliG_C$ and its motility-defective mutants

^1H-^{15}N HSQC spectra of [U-^{15}N] His-*Va* $FliG_C$ (A) and its motility-defective mutants, L270R (B), L271P (C), L259Q (D) and A282T (E). The flagellar motor

profile for each mutant is shown in parenthesis of each spectrum. (CW), clockwise; (CCW), counter-clockwise; (-), nonmotile.

Figure 3. Backbone amide signal assignment of His-*Va* FliG$_{C2}$ and its A282T mutant

^{1}H-^{15}N HSQC spectra of [U-^{15}N] His-*Va* FliG$_{C2}$ (A) and [U-^{15}N] His-*Va* FliG$_{C2}$ (A282T) (B). Sequence specific amide signal assignment was determined by conventional triple resonance NMR experiments for each protein (see Material and Methods).

Figure 4. Chemical shift perturbations of His-*Va* FliG$_{C2}$ induced by the single amino acid replacement A282T

(A) Histogram of chemical shift perturbations. The combined chemical shift changes (Δ, ppm) of amide proton and nitrogen between His-*Va* FliG$_{C2}$ and His-*Va* FliG$_{C2}$(A282T) are plotted against residue number. "Δ" is defined as: $\Delta_{ppm} = [(\Delta\delta H_N)^2 /2 + (\Delta\delta N)^2 /50]^{1/2}$, where δH_N and δN represent chemical shift differences of amide proton and nitrogen between His-*Va* FliG$_{C2}$ and His-*Va* FliG$_{C2}$(A282T), respectively. The red bars indicate the residues whose amide signals disappeared in ^{1}H-^{15}N HSQC spectrum of His-*Va* FliG$_{C2}$(A282T). The secondary structure of His-*Va* FliG$_{C2}$ is indicated at the bottom of the histogram. (B) Mapping of the residues that exhibited chemical shift perturbations induced by the A282T single amino acid replacement. The residues whose $\Delta > 0.2$ ppm

589 and $0.1 < \Delta < 0.2$ ppm are colored in blue and yellow, respectively. The residues
590 whose amide signals disappeared are colored in red.
591
592 **Figure 5. Cluster analysis of the structures of C2 domain of FliGc in the**
593 **MD trajectories**
594 (A, C) Representative conformations of (A) *Va* $FliG_C$ (S1, S2 and S3) and (C)
595 *Va* $FliG_C$(A282T) are shown as ribbon diagrams. Region from G214 to L252 is
596 colored in gray. (B, D) Multi-dimensional scaling (MDS) plots for (B) the *Va*
597 $FliG_C$ and (D) *Va* $FliG_C$(A282T) trajectories. The density in the plot was
598 estimated by the Gaussian kernel-density estimation. Structural data of the
599 colored region (M253-G339) was used for the MDS analysis.
600
601 **Figure 6. Conformational analysis of FliGc domain**
602 (A) Two parameters in the structural domain, the angle (θ) and distance (d)
603 between helices α1 and α4, were used for the analysis. (B) Two dimensional
604 plots of the parameters θ and d for *Va* $FliG_C$ (left panel) and *Va* $FliG_C$ (A282T)
605 (right panel). Each dot depicts the conformation of *Va* FliGc domain in the
606 trajectory. (C) Formation of an additional hydrogen bond between the hydroxyl
607 group of T282 and backbone O of V278 in A282T during the MD simulation.
608 Trajectories at 0 ns (left) and 100 ns (right) after the simulation are shown.
609
610 **Figure 7. Distribution plots of the structural parameters for the structures**
611 **in the MD trajectories**

612 (A) wild type and (B) A282T mutant. The densities of plots were estimated as
613 in Figure 5. The 2D positions of the crystal structures of FliGc: 3ajc, CW-locked
614 mutant in *T. maritima* (Minamino et al., 2011), 1lkv, wild-type in *T. maritima*
615 (Brown et al., 2002); 3usy and 3usw, wild-type in *Helicobacter pylori* (Lam et
616 al., 2012), 4fhr, complexed with FliM, wild-type in *T. maritima* (Vartanian et al.,
617 2012); 3hjl, full-length structure of wild-type in *A. aeulicus* (Lee et al., 2010),
618 are represented as circles in magenta.
619
620
621 **STAR★METHODS**
622 **KEY RESOURCES TABLE**

REAGENT or RESOURCE	SOURCE	IDENTIFIER
Bacterial and Virus Strains		
Escherichia coli DH5α	TaKaRa	Cat#TKR9057
Escherichia coli BL21(DE3)	MERCK	Cat#69450
Chemicals, Peptides, and Recombinant Proteins		
T4 polynucleotide kinase	New England Biolabs	Cat#M0201S
T4 DNA ligase	New England Biolabs	Cat#M0202S
Ammonium ^{15}N chloride	ISOTEC	Cat#299251-10G

D-Glucose [U-13C, 99%]	Cambridge Isotope Laboratories	Cat#CIL-1396-1
Deuterium oxide	Wako	Cat#040-18831
Critical Commercial Assays		
QuikChange Site-Directed Mutagenesis Kit	Agilent	Cat#200518
Deposited Data		
His-Va FliGC_2 Chemical shift data	This paper.	BMRB:12010
His-Va FliGC_2 (A282T) Chemical shift data	This paper	BMRB:12011
Oligonucleotides		
Primer : To construct pCold I-FliG$_{C2}$; ATGTTTGTCTTCGAAAACTTAGTCG	This paper.	N/A
Primer : To construct pCold I-FliG$_{C2}$; CATATGCCTACCTTCGATATGATG	This paper.	N/A
Primer : To construct pCold I-FliG$_{C2}$ (A282T); ACGTGTTGCAAAAAACACTTAAAGGTGCC	Kojima et al., 2011	N/A
Primer : To construct pCold I-FliG$_{C2}$ (A282T); GGCACCTTTAAGTGTTTTTTGCAACACGT	Kojima et al., 2011	N/A
Recombinant DNA		

pCold I	TaKaRa	Cat#TKR3361
Plasmid: pCold I-FliG$_{C}$, See Table 1	Gohara et al., 2014	N/A
Plasmid: pCold I-FliG$_{C2}$, See Table 1	This paper.	N/A
Plasmid: pCold I-FliG$_{C}$(L259Q), See Table 1	Gohara et al., 2014	N/A
Plasmid: pCold I-FliG$_{C}$(L270R), See Table 1	Gohara et al., 2014	N/A
Plasmid: pCold I-FliG$_{C}$(L271P), See Table 1	Gohara et al., 2014	N/A
Plasmid: pCold I-FliG$_{C}$(A282T), See Table 1	This paper.	N/A
Plasmid: pCold I-FliG$_{C2}$(A282T), See Table 1	This paper.	N/A
Software and Algorithms		
MODELLER 9.16	Marti-Renom et al. 2000	https://salilab.org/modeller/
ALAdeGAP	Hijikata et al., 2011	http://cib.cf.ocha.ac.jp/aladegap/
GROMACS ver 4.6.2	Pronk et al. 2013	http://www.gromacs.org
TopSpin 3.2	Bruker Biospin	https://www.bruker.com/products/mr/nmr/nmr-software/software/topspin/overview.html

Sparky	T. D. Goddard and D. G. Kneller, SPARKY 3, University of California, San Francisco	https://www.cgl.ucsf.edu/home/sparky/
TALOS-N	Shen and Bax, 2015	https://spin.niddk.nih.gov/bax/software/TALOS-N/
NMRPipe	Delaglio et al., 1995	https://spin.niddk.nih.gov/bax/software/NMRPipe/
Other		

CONTACT FOR REAGENT AND RESOURCE SHARING

Further information and requests for resources and reagents should be directed to and will be fulfilled by the Lead Contact, Michio Homma (g44416@cc.nagoya-u.ac.jp)

EXPERIMENTAL MODEL AND SUBJECT DETAILS

Strains Used in Protein Production

The FliG protein fragments used in this study were manipulated and expressed in *Escherichia coli* DH5α and *Escherichia coli* BL21 (DE3), respectively. These strains were transformed with pCold I expression vector (TaKaRa).

METHODS DETAILS

Protein expression in *E. coli* and purification

Strains and plasmids used in this study are shown in Table 1. Routine DNA manipulation was performed using *E. coli* DH5α according to the protocols described previously. pCold I-FliG_C(A282T) was constructed by QuikChange method (Stratagene), using pCold I-FliG_C as a template; pCold I-FliG_{C2} and pCold I-FliG_{C2}(A282T) were constructed by an inverse PCR-based method. First, the deletion fragments whose templates were pCold I-FliG_C and pCold I-FliG_C(A282T) were amplified by PCR. The fragments were subjected to agarose gel electrophoresis and extracted using a DNA extraction kit (Qiagen). The 5'-hydroxyl termini of the extracted products were phosphorylated using T4 polynucleotide kinase (NEB). DNA ligation was performed using T4 DNA ligase (NEB). After stopping the reaction by heating, these plasmids were introduced into *E. coli* DH5α. All plasmids were purified and sequenced to confirm the insertions. The expression plasmids were introduced into *E. coli*

653 BL21(DE3). The *E. coli* cells were cultured in LB medium containing 1 % (w/v)
654 Bactotryptone, 0.5 % (w/v) yeast extract, and 0.5 % (w/v) NaCl. Each sample
655 was confirmed by SDS-PAGE. The samples were prepared by mixing with SDS
656 sample buffer and heating at 95 ºC for 5 min. The samples were subjected to
657 SDS-PAGE on 14 % polyacrylamide gels and detected by Coomassie Brilliant
658 Blue staining.
659 His-*Va* $FliG_C$ [(U-^{13}C,^{15}N) His-*Va* $FliG_C$] proteins uniformly labeled
660 with ^{13}C and ^{15}N were prepared according to the procedure described previously,
661 with slight modification (Gohara *et al.*, 2014). Briefly, *E. coli* was cultured at 37
662 ºC as first culture in 200 mL of M9 medium [7.0 g/L Na_2HPO_4 (anhydrous), 3.0
663 g/L KH_2PO_4 (anhydrous), 0.50 g/L NaCl, 1.0 g/L [U-^{13}C] -glucose, 0.50 g/L
664 $^{15}NH_4Cl$, 20 mg/L adenine, 20 mg/L thymine, 20 mg/L guanosine, 20 mg/L
665 cytidine, 20 mg/L thiamin hydrochloride, 20 mg/L (+)-Biotin, 33 μM $FeCl_3$, 1.0
666 mM $MgSO_4$, 50 μM $MnCl_2$, 0.10 mM $CaCl_2$] containing ampicillin, to a final
667 concentration of 100 μg/mL. The first culture was inoculated into 2 L M9
668 medium and was incubated at 37 ºC. When the cell density at OD_{660} reached
669 about 0.4, IPTG (isopropyl-β-D-thiogalactopyranoside) was added to a final
670 concentration of 0.5 mM and the incubation was continued for approximately 18
671 h at 16 ºC. The cells were harvested by centrifugation and stored frozen at -80
672 ºC. The cells were thawed and suspended in buffer A [50 mM Tris-HCl (pH 8.0),
673 150 mM NaCl, 5 mM imidazole] containing protease inhibitor, cOmplete,
674 EDTA-free (Roche Life Science). The cells were disrupted by sonication (Power
675 8, duty cycle 50 %). Unbroken cells were removed by centrifugation. The

supernatant was ultracentrifuged at 100,000 *g* for 30 min. The resultant supernatant was mixed with Ni-NTA Agarose (Qiagen), and incubated for 1 h at 4 ºC with shaking and was loaded on to a polypropylene column by batch method. After the column was washed twice with buffer B [50 mM Tris-HCl (pH 8.0), 150 mM NaCl, 20 mM imidazole], the proteins were eluted into four fractions with buffer C [50 mM Tris-HCl (pH 8.0), 150 mM NaCl, 500 mM imidazole]. This method was applied to prepare unlabeled $FliG_C$ proteins.

The purified proteins were concentrated to about 500 μL using Amicon device (Millipore) and subjected to size exclusion chromatography using Superdex 200 Increase 10/300 (GE Healthcare) in buffer D [50 mM Tris-HCl (pH 8.0), 150 mM NaCl]. The flow rate was 0.75 mL/min. The peak fractions were collected and concentrated as described above. The proteins were subjected to buffer exchange with buffer E [50 mM Tris-HCl (pH 8.0), protease inhibitor, cOmplete, EDTA-free]. Protein concentration was determined using Direct Detect spectrophotometer (Millipore).

NMR Spectroscopy

The [U-^{13}C,^{15}N] His-*Va* $FliG_C$ protein and its mutants were concentrated to 0.9 mM. The NMR sample buffer contained 50 mM Tris-HCl, 150 mM NaCl, cOmplete EDTA-free, 0.01% (w/v) sodium 2,2-dimethyl-2-silapentane-5-sulfonate (DSS) (Cambridge Isotope Laboratories, Inc.) and 5% (w/v) D_2O at pH 7.0. NMR measurements were performed on an

AV-III 600 spectrometer (Bruker Biospin) equipped with a TCI triple resonance cryogenic probe at 288K.

The following NMR experiments were performed to assign backbone resonances of His-*Va* $FliG_{C2}$ and its mutants: 3D HNCACB, CBCACONH, HNCA, HNCOCA, HNCO, HNCACO and 2D ^{1}H-^{15}N HSQC. Backbone ^{15}N T_2 spectra were recorded for His-*Va* $FliG_{C2}$ and His-*Va* $FliG_{C2}$(A282T), using standard CPMG pulse sequence with nine different delay times; t = 0, 17, 34, 51, 68, 85, 102, 119 and 136 ms. T_2 value was obtained by fitting signal intensities from each spectrum to a single exponential curve. All NMR spectra were processed with TopSpin (Bruker Biospin), NMRPipe (Delaglio *et al.*, 1995) and Sparky (Goddard and Kneller, University of California, San Francisco).

Secondary structure analysis

Protein backbone dihedral angles (φ,ψ) of His-*Va* $FliG_{C2}$ and His-*Va* $FliG_{C2}$(A282T) were calculated from chemical shift value of ^{1}HN, ^{15}NH, $^{13}C\alpha$, $^{13}C\beta$ and ^{13}CO, using TALOS-N program (Shen and Bax, 2015).

Homology modeling

A model structure of *Va* $FliG_C$ was built using MODELLER version 9.16 (Marti-Renom *et al.*, 2000), using the crystal structure of FliG from *T. maritima* (PDB code: 1lkv) as template and sequence alignment of the two amino acid sequences generated by ALAdeGAP (Hijikata *et al.*, 2011). Model structures of

720 mutant *Va* $FliG_C$ proteins with single amino acid substitutions (L259Q, L271P
721 or A282T) were built based on the model structure of the wild type.
722
723 **Molecular dynamics simulation**
724 MD simulations were performed using GROMACS version 4.6.2 (Pronk *et al.*,
725 2013). The topology was generated with standard amino acid protonation states
726 at pH 7.0. The force field of AMBER99SB-ILDN and the water model of TIP3P
727 model were used for the simulation. The starting structure was placed in a cubic
728 box with 1.2 nm spaces around the solute and the box was filled with water
729 molecules. Na^+ ions were added to a concentration of 150 mM. Finally, Cl^- ions
730 were added to make the total electrical charge neutral. There was a total of
731 52,873 atoms in the simulation. Energy minimization was performed by the
732 steepest descent method. Following energy minimization, the system was
733 equilibrated for 100 ps at 300 K under NVT (constant number of particles,
734 volume and temperature) and NPT (constant number of particles, pressure and
735 temperature) conditions. After equilibration, an all atom molecular dynamics
736 simulation at 300 K under the NPT condition was performed for 500 ns. Each
737 *Va* $FliG_C$ protein was simulated thrice independently.
738
739 **QUANTIFICATION AND STATISTICAL ANALYSIS**
740 The ^{15}N T_2 values of His-*Va* $FliG_{C2}$ and His-*Va* $FliG_{C2}$ (A282T) (Figure S2)
741 were obtained by fitting the intensities of the peak heights to an exponential

curve using a nonlinear least squares fitting method in Sparky (Goddard and Kneller, University of California, San Francisco).

DATA AND SOFTWARE AVAILABILITY

Data Resources

The resonance assignments for His-*Va* $FliG_{C2}$ (Table S1) and His-*Va* $FliG_{C2}$ (A282T) (Table S2) deposited in the BioMagResBank (BMRB; http://www.bmrb.wisc.edu) under accession numbers 12010 and 12011, respectively.

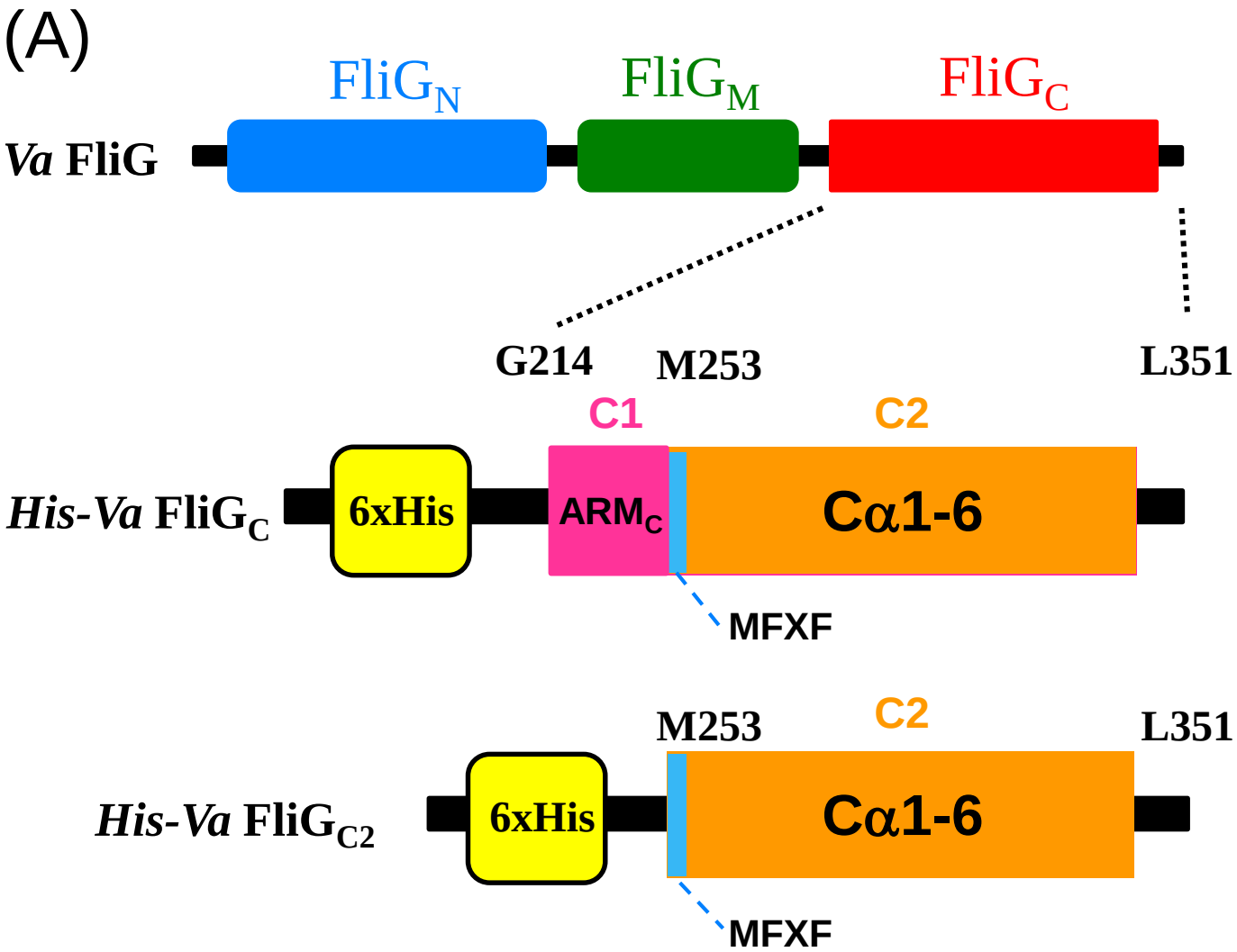

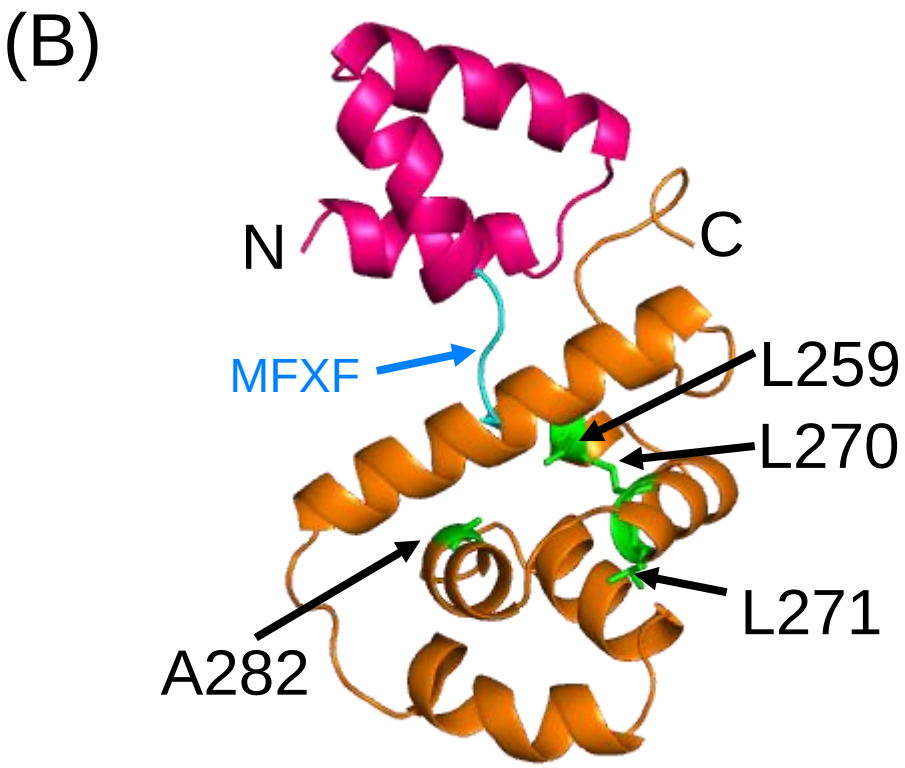

Figure 1. Miyanoiri *et al.*

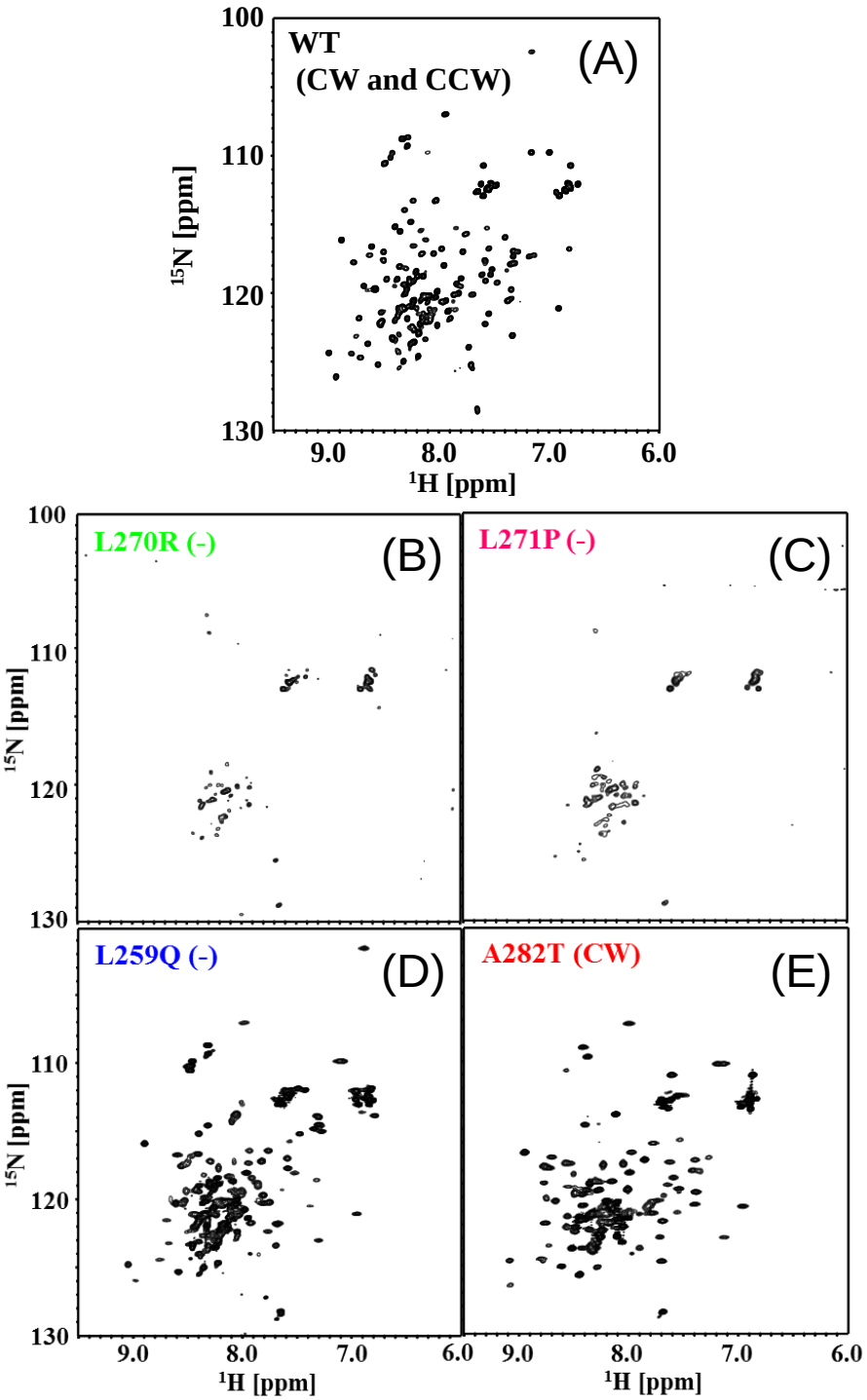

Figure 2. Miyanoiri *et al*.

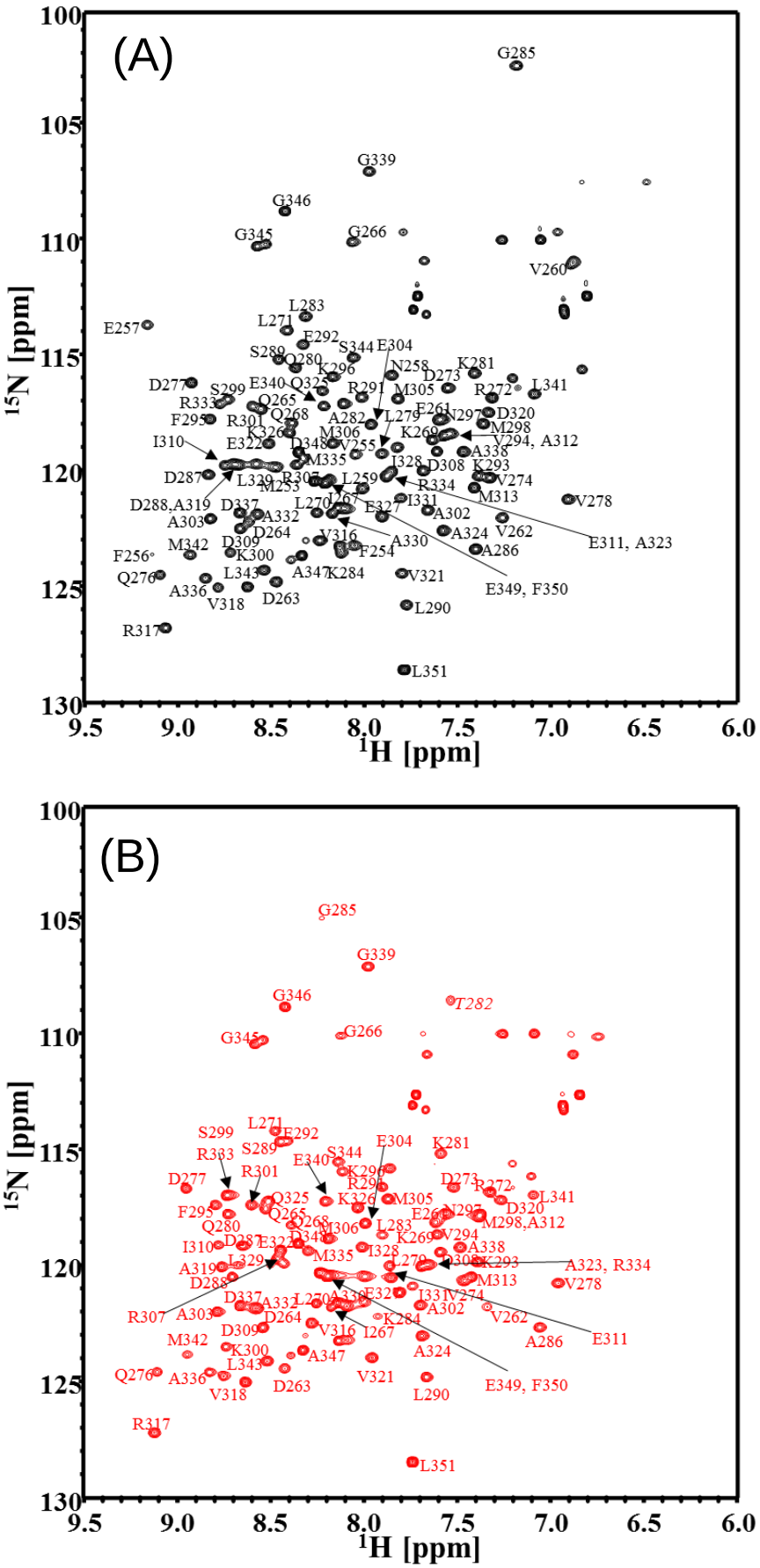

Figure 3. Miyanoiri *et al*.

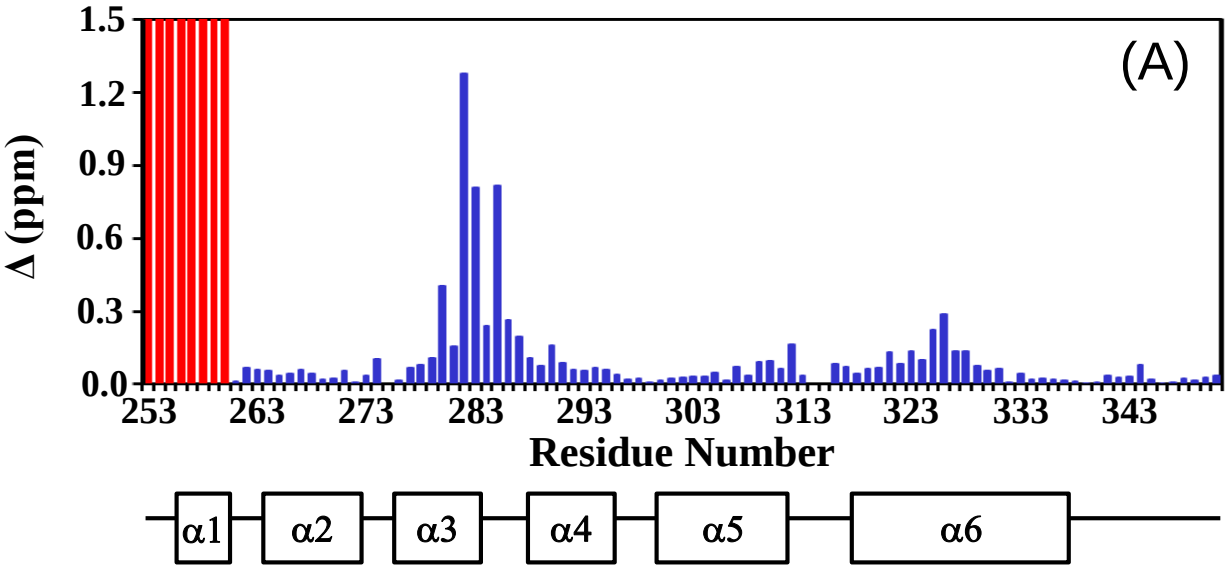

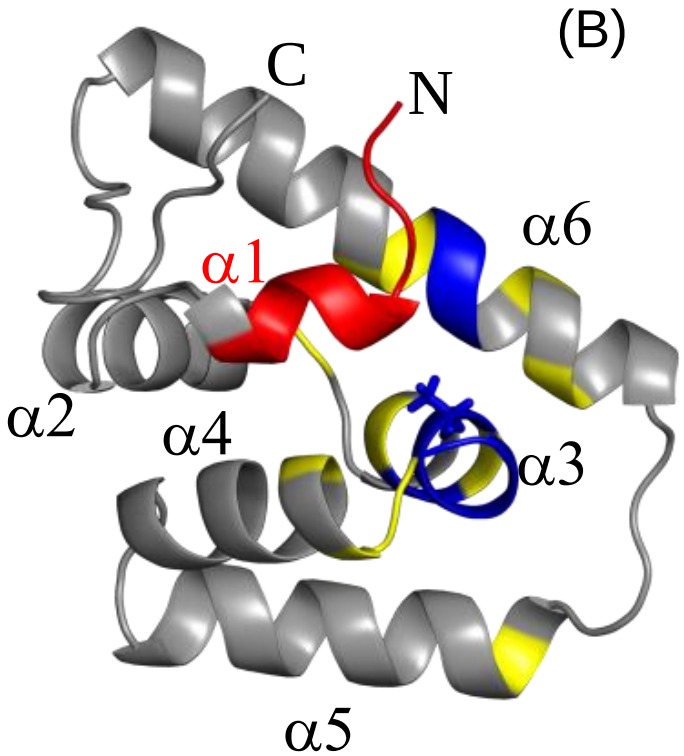

Figure 4. Miyanoiri *et al*.

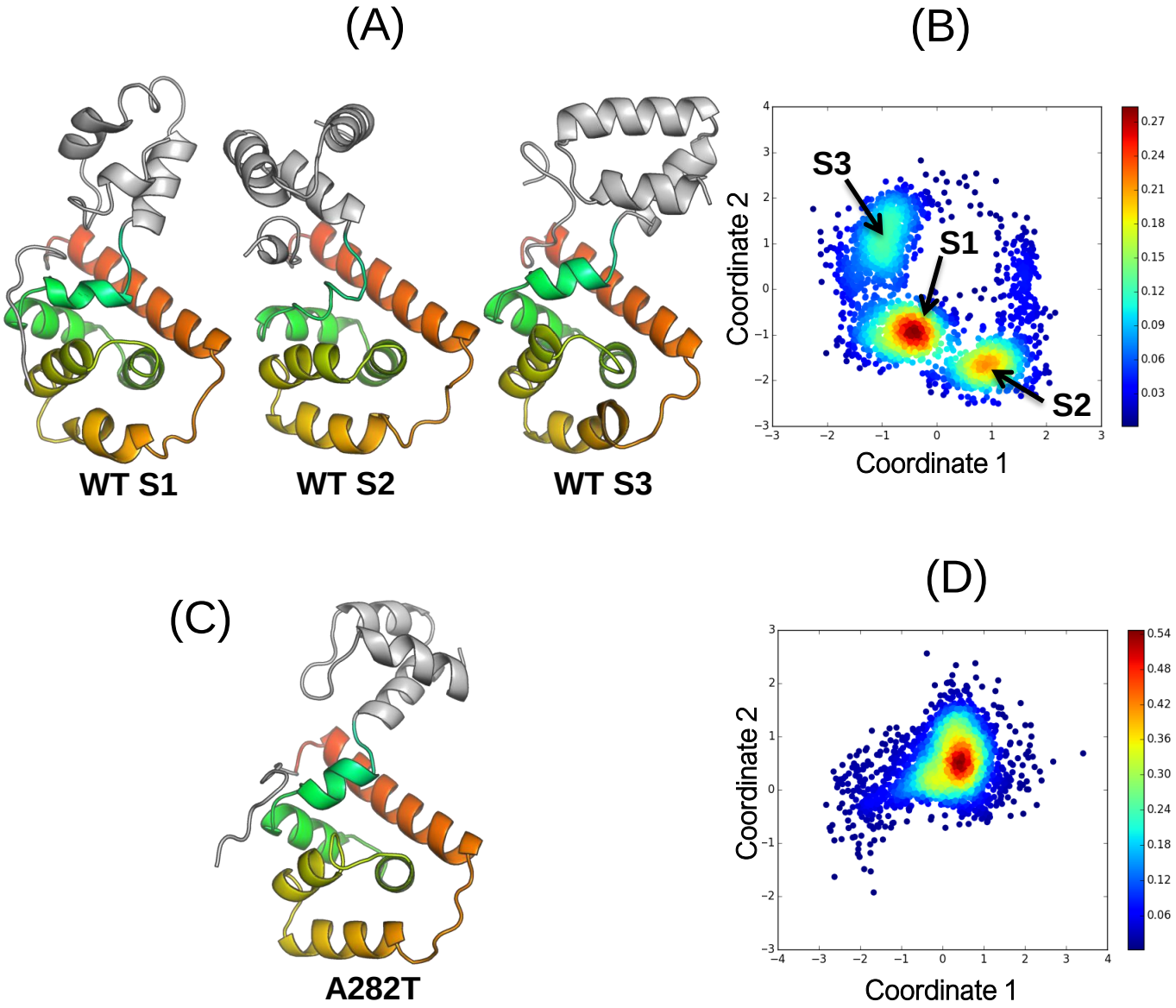

Figure 5. Miyanoiri *et al*.

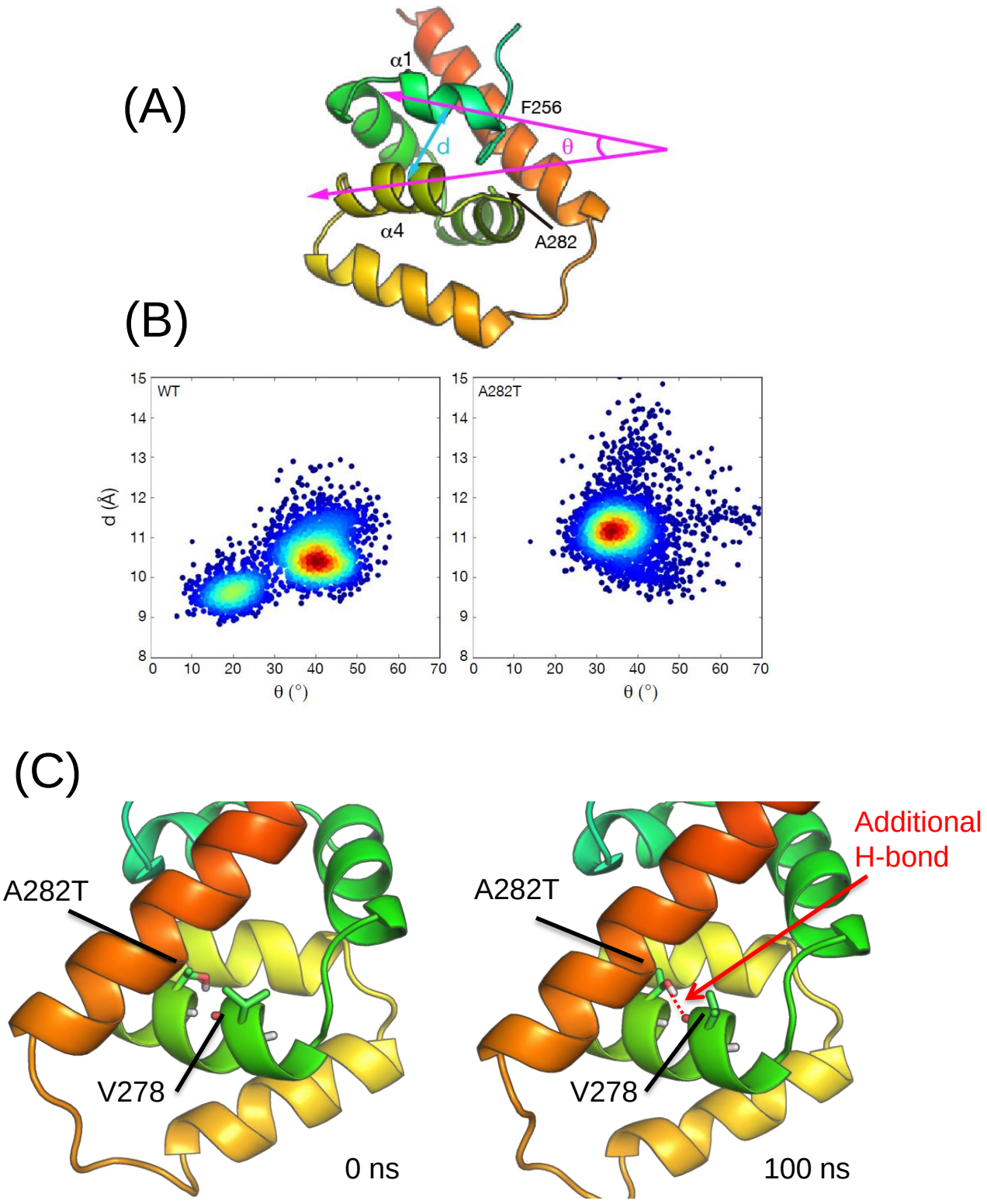

Figure 6. Miyanoiri *et al*.

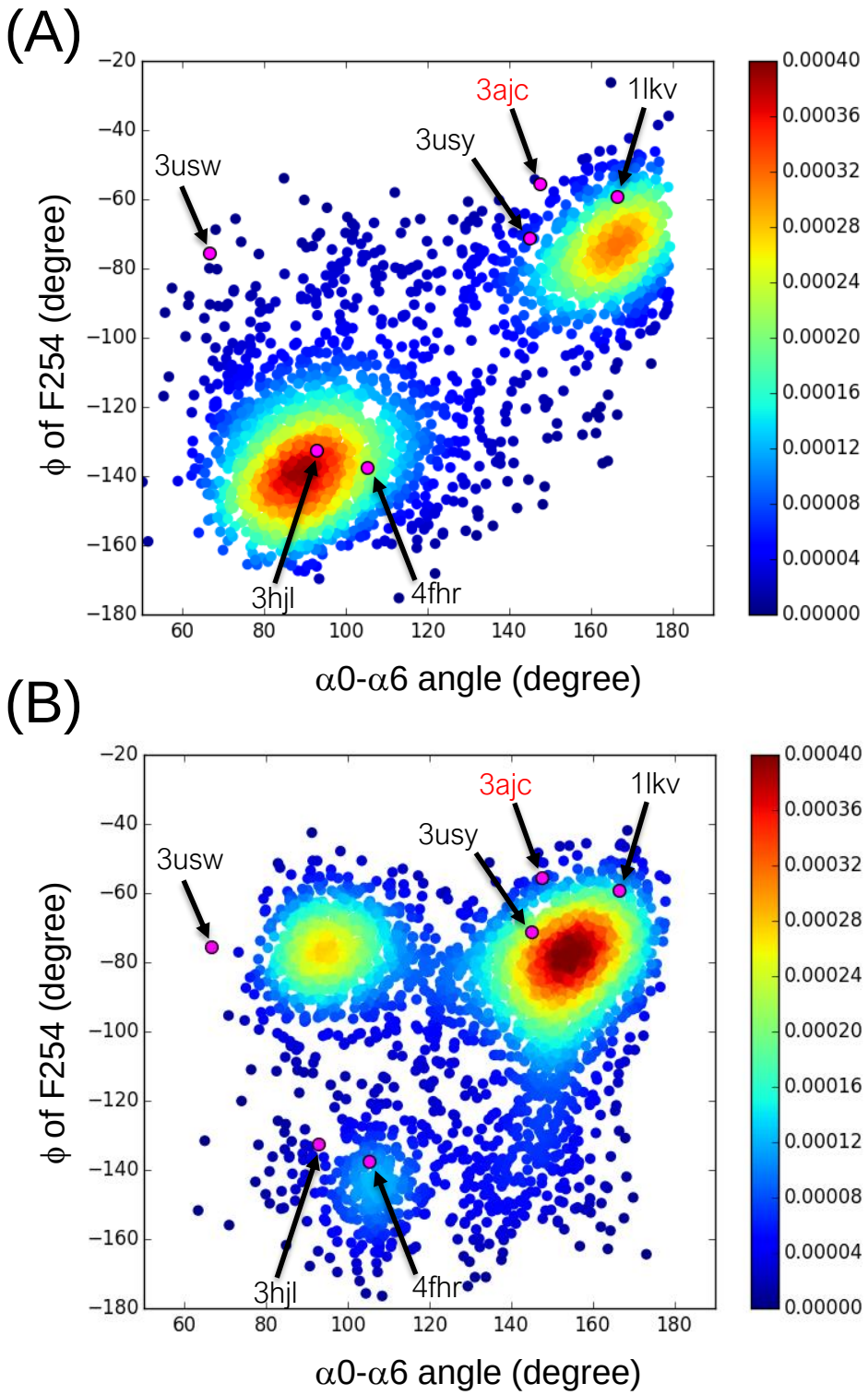

Figure 7. Miyanoiri *et al*.

Supplemental Information

Structural and functional analysis of the C-terminal region of FliG, an essential motor component of *Vibrio* Na^+-driven flagella

Yohei Miyanoiri, Atsushi Hijikata,Yuuki Nishino, Mizuki Gohara, Yasuhiro Onoue, Seiji Kojima, Chojiro Kojima, Tsuyoshi Shirai, Masatsune Kainosho and Michio Homma

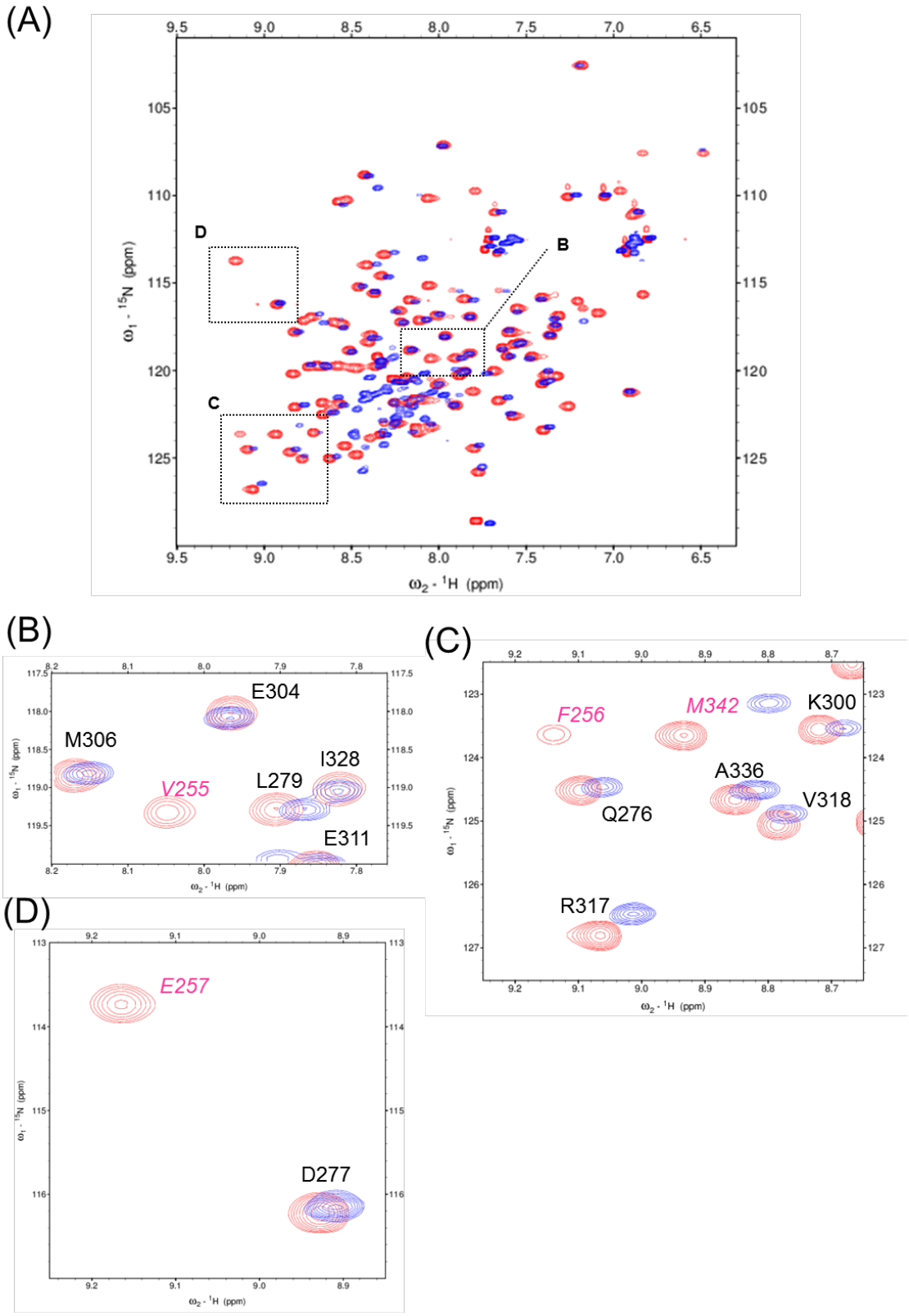

Figure S1. Related to Figure 2. Comparison of ^{1}H-^{15}N HSQC spectra between His-*Va* FliG$_C$ and His-*Va* FliG$_{C2}$. (A) Overlay of ^{1}H-^{15}N HSQC spectra of His-*Va* FliG$_C$ (blue) and His-*Va* FliG$_{C2}$ (red). Although amino acid residues in His-*Va* FliG$_C$ is 40 more than that of His-*Va* FliG$_{C2}$, observed amide signals in ^{1}H-^{15}N HSQC spectra are almost same between them. It is suggested that some amide signals in His-*Va* FliG$_C$ were broadened to invisibility. (B)-(D) The enlarged spectra of B-D region (dotted square) in (A), respectively. Amide signals which are assigned both His-*Va* FliG$_C$ and His-*Va* FliG$_{C2}$ are labeled with black character. On the other hand, the residues which could be assigned in only His-*Va* FliG$_{C2}$, are shown in pink italic characters. Amide signals of V255(B), F256(C) and E257(D) could not be observed in His-*Va* FliG$_C$.

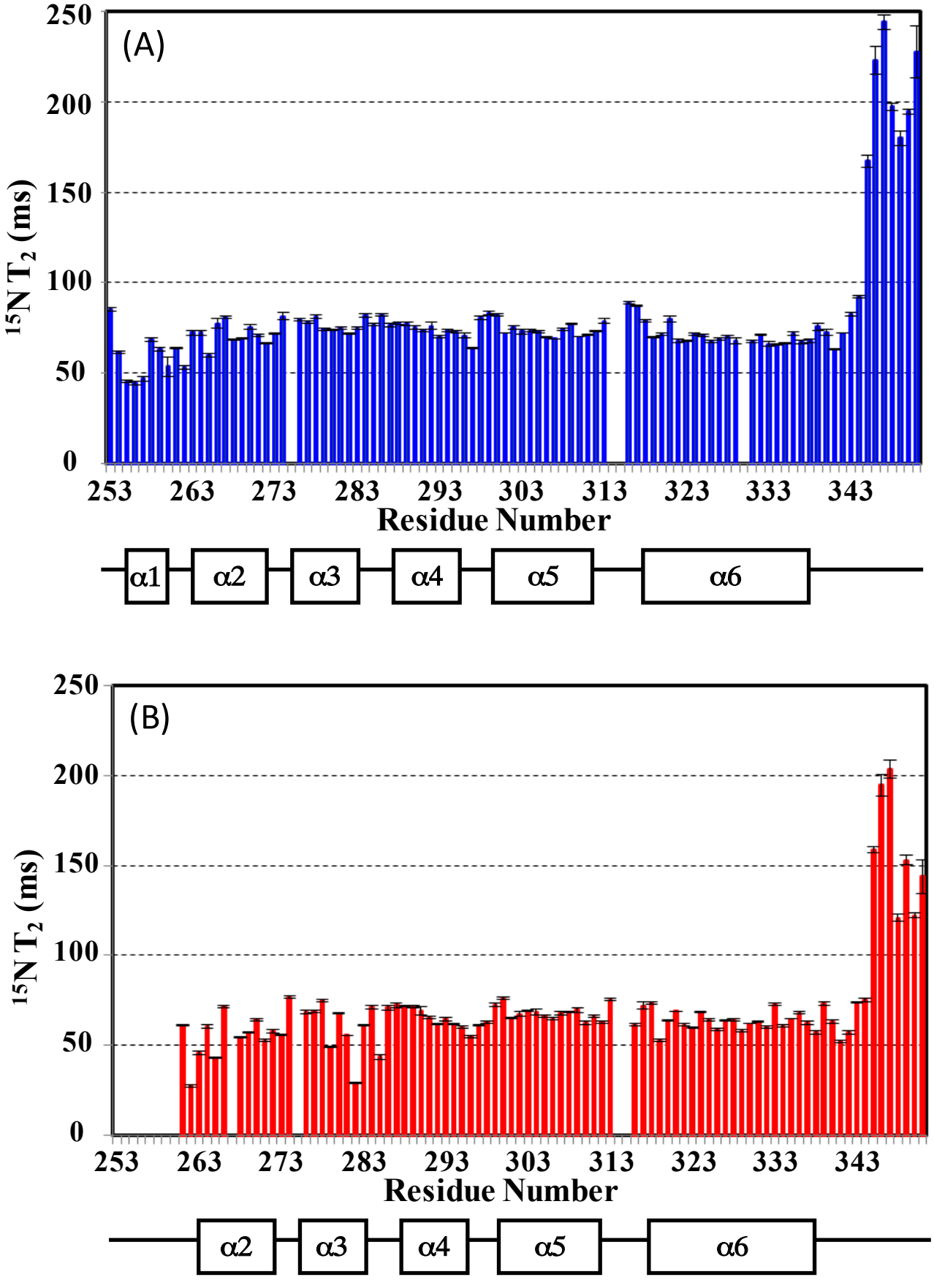

Figure S2. Related to Figure 3. Comparison between the backbone dynamics of His-*Va* FliG$_{C2}$ and His-*Va* FliG$_{C2}$(A282T). ^{15}N T$_2$ values of His-*Va* FliG$_{C2}$ (A) and His-*Va* FliG$_{C2}$ (A282T) (B), with error bars as a function of the residue number. The secondary structures of His-*Va* FliG$_{C2}$ and His-*Va* FliG$_{C2}$ (A282T) are indicated at the bottom of each plot.

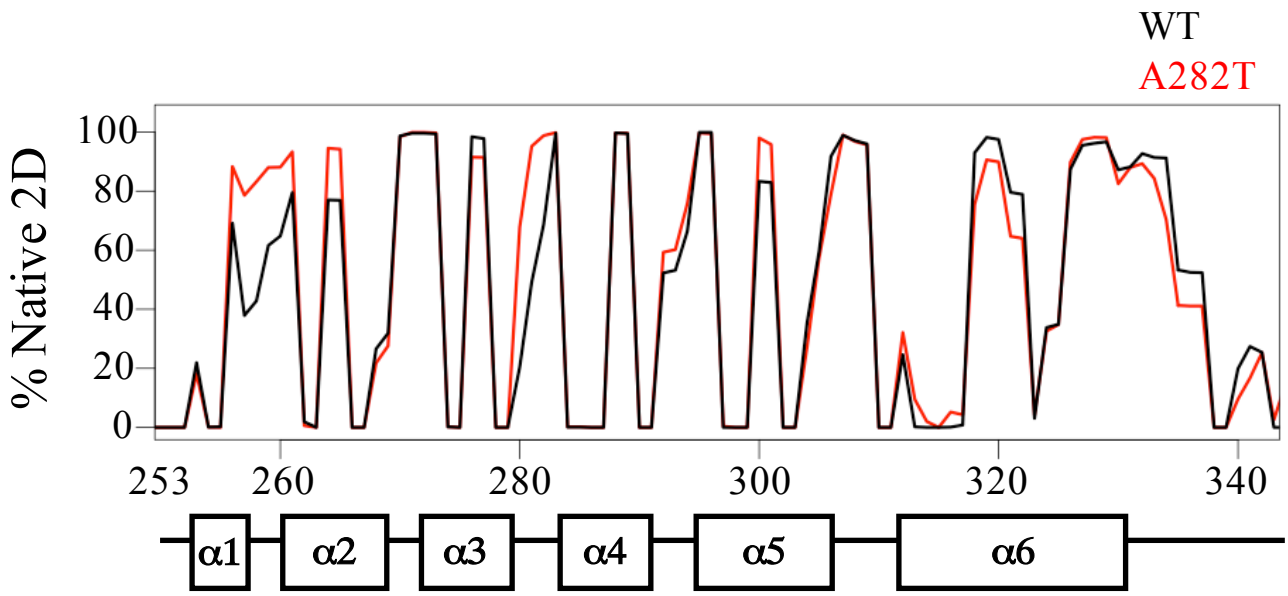

Figure S3. Related to Figure 5. The fraction of amino acid residues, whose native secondary structure was retained during the MD simulation. Black and red lines indicate the fractions for wild-type and A282T mutant of $FliG_C$ domains, respectively. The secondary structures of $FliG_C$ are indicated at the bottom of the plot.

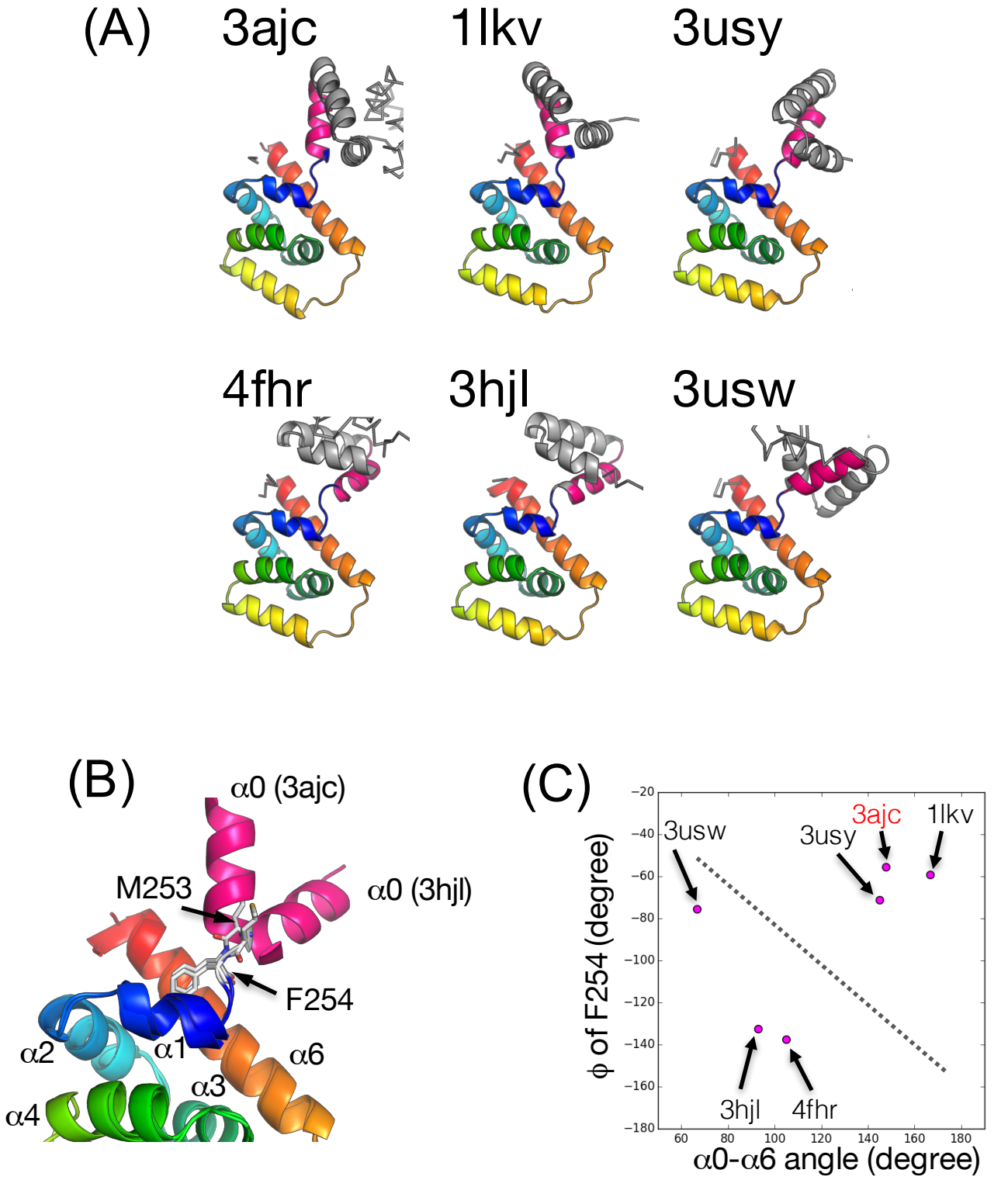

Figure S4 . Related to Figure 7. Rearrangement patterns of the crystal structures of FliG$_C$. (A) The crystal structures of FliG$_C$: 3ajc, CW-locked mutant in *T. maritima* [11], 1lkv, wild-type in *T. maritima* [21]; 3usy and 3usw, wild-type in *Helicobacter pylori* [26], 4fhr, complexed with FliM, wild-type in *T. maritima* [12]; 3hjl, full-length structure of wild-type in *A. aeulicus* [22]. (B) The rearrangement of helix α0 and the hinge between ARM$_C$ and Cα1-6 domain of FliG$_C$ in two crystal structures (3ajc and 3hjl). The residue numbers are according to those of *V. alginolyticus*. (C) The 2D plots of the two structural parameters for the rearrangement of ARM$_C$ and Cα1-6 domains. Each dot in the plot depicts the individual crystal structure.

Table S1. Related to Figure 3. ^{1}H, ^{13}C and ^{15}N chemical shift and predicted dihedral angles of U-^{13}C,^{15}N His-*Va* $FliG_{C2}$ backbone at 288K, pH 7.0.

	Chemical shift [ppm] *1					dihedral angle [°] *2		secondary structure *3
	^{13}CO	$^{13}C\alpha$	$^{13}C\beta$	^{15}NH	^{1}HN	Phi	Psi	
M253	175.1	54.95	32.13	119.9	8.473	-	-	L
F254	175.0	58.54	39.89	123.3	8.054	-72.16	140.8	H
V255	176.4	59.95	34.45	119.3	8.051	-107.5	159.0	L
F256	176.1	63.17	39.65	123.7	9.140	-57.32	-42.01	H
E257	178.0	59.59	28.40	113.7	9.168	-66.21	-32.88	H
N258	176.5	54.89	38.76	115.9	7.850	-70.97	-33.33	H
L259	177.4	57.82	41.29	120.8	8.012	-65.07	-37.95	H
V260	175.6	64.42	31.78	111.1	6.892	-70.78	-17.10	H
E261	177.0	56.10	30.07	117.9	7.602	-90.85	-6.492	L
V262	174.7	62.58	31.84	122.0	7.256	-74.39	147.5	L
D263	176.3	54.42	41.53	124.8	8.473	-66.57	153.4	L
D264	177.8	58.73	40.75	122.2	8.623	-57.85	-39.97	H
Q265	178.9	59.56	27.96	117.4	8.555	-64.61	-38.99	H
G266	175.4	47.48	-	110.2	8.065	-64.85	-41.54	H
I267	177.9	62.21	34.82	121.7	8.102	-68.96	-34.99	H
Q268	179.0	60.23	27.71	118.0	8.389	-64.68	-41.20	H
K269	178.8	59.76	32.43	118.7	7.637	-65.98	-39.88	H
L270	178.4	58.43	42.47	121.9	8.256	-65.46	-44.39	H
L271	179.1	57.08	41.59	114.0	8.415	-68.64	-25.00	H
R272	177.5	58.92	30.39	116.9	7.311	-71.53	-28.53	H
D273	175.8	54.22	42.63	116.4	7.554	-96.25	-6.026	L
V274	173.8	59.97	33.40	120.4	7.323	-98.90	135.8	L
P275	177.9	62.90	32.78	not assigned	-	-62.47	147.8	L
Q276	177.1	60.14	28.87	124.5	9.094	-56.64	-40.29	H
D277	178.1	56.82	39.72	116.2	8.925	-63.10	-34.34	H
V278	177.4	65.67	32.21	121.3	6.909	-70.40	-42.90	H
L279	178.0	58.23	41.82	119.3	7.905	-63.27	-41.37	H
Q280	177.7	60.20	28.56	115.6	8.370	-61.77	-42.50	H
K281	177.3	60.62	33.38	115.8	7.407	-66.08	-41.95	H
A282	180.1	54.82	19.68	117.1	8.112	-65.18	-39.79	H
L283	180.0	55.94	42.13	113.3	8.315	-71.69	-23.15	H
K284	177.4	58.24	31.21	123.6	8.127	-69.49	-23.60	L
G285	173.0	44.96	-	102.5	7.179	-94.84	1.975	L
A286	176.2	50.62	22.13	123.4	7.401	-111.8	146.4	L
D287	176.3	53.41	42.12	120.3	8.835	-68.98	157.3	L
D288	178.1	58.20	40.94	119.8	8.675	-60.55	-37.56	H
S289	177.0	61.88	not assigned	115.2	8.459	-65.02	-39.80	H
L290	178.5	57.53	41.06	125.9	7.771	-67.92	-42.67	H
R291	176.9	60.72	29.93	116.8	8.016	-61.80	-42.60	H
E292	178.7	59.10	28.79	114.6	8.328	-64.44	-38.32	H
K293	177.3	58.19	32.50	120.3	7.384	-67.20	-40.96	H
V294	178.2	67.07	30.97	118.4	7.541	-65.48	-43.67	H
F295	179.0	58.46	37.77	117.9	8.827	-67.63	-22.82	H
K296	176.4	58.24	31.62	116.0	8.172	-73.47	-19.63	H
N297	172.6	54.47	41.25	117.8	7.590	-111.3	-15.03	L
M298	175.3	54.73	37.29	118.0	7.358	-128.0	148.8	L
S299	174.5	58.49	63.82	116.9	8.732	-69.28	156.8	L
K300	179.2	60.27	32.45	123.6	8.720	-57.90	-39.45	H
R301	178.4	58.40	29.69	117.2	8.601	-67.20	-37.91	H
A302	180.9	54.99	18.45	121.8	7.662	-65.44	-41.43	H
A303	179.2	55.34	18.92	122.1	8.826	-65.22	-40.32	H
E304	178.9	59.40	29.40	118.1	7.963	-64.01	-43.13	H
M305	177.9	58.79	33.12	116.9	7.817	-65.96	-42.13	H
M306	177.8	58.52	31.62	118.9	8.172	-64.36	-43.01	H
R307	179.2	60.34	29.77	119.8	8.361	-62.73	-43.01	H
D308	179.1	57.22	39.90	119.2	7.614	-66.41	-41.27	H
D309	179.9	57.55	40.00	122.5	8.668	-63.47	-40.71	H
I310	178.4	65.46	38.15	119.8	8.751	-64.61	-38.35	H
E311	177.6	58.63	29.27	120.1	7.853	-70.56	-19.04	H
A312	177.9	52.55	19.53	118.5	7.575	-88.15	-7.150	L
M313	173.7	55.17	33.33	120.8	7.409	-73.31	139.0	L
P314	not assigned	not assigned	not assigned	not assigned	-	-67.38	151.6	L
P315	176.3	63.83	31.92	not assigned	-	-62.14	141.9	L
V316	176.1	60.10	34.07	123.1	8.240	-104.7	137.3	L
R317	178.4	56.54	30.37	126.9	9.063	-71.57	137.1	L
V318	178.0	67.09	31.43	125.1	8.785	-55.43	-42.33	H
A319	180.7	55.02	18.46	119.7	8.704	-63.50	-36.02	H
D320	179.2	56.68	40.59	117.5	7.329	-70.57	-38.36	H
V321	178.3	66.96	31.94	124.5	7.796	-65.25	-43.39	H
E322	179.1	59.69	29.29	118.9	8.512	-64.06	-39.72	H
A323	180.4	55.24	18.14	120.3	7.878	-65.41	-40.27	H
A324	179.4	55.14	18.82	122.6	7.580	-67.03	-41.51	H
Q325	178.4	59.52	27.20	116.6	8.228	-65.21	-39.41	H
K326	179.5	60.07	32.36	118.4	8.400	-64.69	-40.79	H
E327	179.2	59.57	28.97	122.0	7.904	-65.42	-42.99	H
I328	177.8	66.16	37.30	119.1	7.819	-63.63	-42.46	H
L329	178.1	57.93	41.89	119.8	8.582	-64.90	-39.85	H
A330	181.3	55.40	17.75	121.9	8.172	-64.23	-39.78	H
I331	178.0	65.58	38.57	121.2	7.802	-65.77	-43.88	H
A332	179.2	55.20	17.55	121.9	8.573	-63.81	-38.35	H
R333	178.1	59.72	30.05	117.2	8.776	-64.22	-42.19	H
R334	180.1	59.77	29.59	120.1	7.686	-65.21	-41.98	H
M335	178.7	59.59	33.88	119.5	8.329	-64.66	-43.74	H
A336	182.2	54.89	17.80	124.7	8.851	-61.73	-40.56	H
D337	177.5	57.17	40.15	121.9	8.670	-66.12	-27.17	H
A338	177.7	52.15	19.29	119.2	7.470	-83.33	-5.619	L
G339	175.0	45.66	-	107.0	7.973	79.61	15.52	L
E340	175.0	56.64	31.25	117.2	8.221	-93.08	-10.26	L
L341	174.4	53.91	45.43	116.7	7.089	-134.3	138.9	E
M342	175.1	54.32	33.14	123.7	8.931	-101.9	123.5	E
L343	176.6	54.39	41.61	124.4	8.538	-79.23	136.2	E
S344	174.7	58.26	64.12	115.1	8.060	-79.73	152.5	L
G345	174.7	45.42	-	110.3	8.575	-174.0	163.2	L
G346	174.0	45.21	-	108.8	8.423	91.77	2.762	L
A347	177.6	52.66	19.35	123.7	8.336	-89.06	-8.814	L
D348	176.2	54.59	41.16	119.2	8.353	-72.33	-18.32	L
E349	175.9	56.77	30.39	120.6	8.212	-87.52	-8.306	L
F350	174.8	57.47	39.46	120.5	8.267	-84.13	138.9	L
L351	182.4	56.78	43.52	128.6	7.785	-	-	L

*1 ^{1}H, ^{13}C and ^{15}N chemical shifts are referenced indirectly against DSS.
*2 The backbone dihedral angles (phi and psi) for each residue are predicted from chemical shift data using TALOS-N [23].
*3 The secondary structure was predicted from TALOS-N [23].
H:α-helix; E: β-strand; L: coil

Table S2. Related to Figure 3. ^{1}H, ^{13}C and ^{15}N chemical shift and predicted dihedral angles of U-^{13}C,^{15}N His-*Va* FliG $_{C2}$ (A282T) backbone at 288K, pH 7.0.

	Chemical shift [ppm] *1					dihedral angle [°] *2		secondary structure *3
	^{13}CO	$^{13}C\alpha$	$^{13}C\beta$	^{15}NH	^{1}HN	Phi	Psi	
M253	not assigned	not assigned	not assigned	not assigned	not assigned	-	-	-
F254	not assigned	not assigned	not assigned	not assigned	not assigned	-	-	-
V255	not assigned	not assigned	not assigned	not assigned	not assigned	-	-	-
F256	not assigned	not assigned	not assigned	not assigned	not assigned	-	-	-
E257	not assigned	not assigned	not assigned	not assigned	not assigned	-	-	-
N258	not assigned	not assigned	not assigned	not assigned	not assigned	-	-	-
L259	not assigned	not assigned	not assigned	not assigned	not assigned	-	-	-
V260	175.557	64.179	not assigned	not assigned	6.893	-	-	L
E261	177.101	56.089	30.131	117.932	7.593	-91.614	-0.783	L
V262	174.749	62.823	31.833	121.825	7.332	-68.889	143.369	L
D263	176.152	54.324	41.357	124.494	8.425	-69.403	150.139	L
D264	177.755	58.552	40.826	121.869	8.59	-58.451	-38.85	H
Q265	178.866	59.411	28.037	117.596	8.527	-64.987	-39.502	H
G266	175.471	47.476	-	110.083	8.125	-65.735	-42.18	H
I267	177.819	62.329	34.988	121.803	8.175	-68.764	-34.633	H
Q268	179.018	60.083	27.768	118.245	8.39	-64.317	-40.947	H
K269	178.733	59.755	32.249	118.687	7.608	-66.082	-40.017	H
L270	178.488	58.515	42.242	121.689	8.256	-65.939	-43.579	H
L271	178.932	57.123	41.468	114.187	8.474	-67.043	-23.39	H
R272	177.532	58.83	30.398	116.844	7.316	-72.282	-28.99	H
D273	176.082	54.457	42.645	116.624	7.516	-95.825	-6.608	L
V274	173.683	60.025	33.228	120.692	7.455	-99.466	132.524	L
P275	177.909	63.005	32.701	not assigned	-	-61.634	146.665	L
Q276	177.383	60.068	28.851	124.602	9.106	-57.123	-39.645	H
D277	178.005	56.916	39.781	116.687	8.952	-62.574	-34.114	H
V278	178.192	65.654	32.208	120.743	6.957	-70.502	-42.445	H
L279	179.422	58.111	41.897	120.054	7.858	-66.052	-40.894	H
Q280	177.693	60.447	28.379	117.862	8.731	-62.572	-42.038	H
K281	177.648	60.429	33.552	115.176	7.586	-65.88	-42.218	H
T282	176.288	65.453	68.566	108.579	7.533	-65.09	-37.731	H
L283	179.378	56.182	42.796	118.711	7.897	-74.64	-24.487	H
K284	177.191	58.702	31.543	122.178	7.923	-65.402	-25.803	L
G285	173.755	44.723		105.017	8.225	-95.907	3.008	L
A286	176.414	51.306	21.315	122.723	7.058	-86.16	152.387	L
D287	176.448	53.561	42.126	119.182	8.651	-67.671	155.918	L
D288	178.044	58.1	40.971	120.519	8.707	-59.295	-37.861	H
S289	176.963	61.881	not assigned	114.62	8.451	-64.539	-40.626	H
L290	178.184	57.799	40.969	124.812	7.667	-69.323	-42.614	H
R291	176.976	60.606	30.205	116.606	7.899	-61.683	-42.764	H
E292	178.802	59.089	28.882	114.602	8.412	-64.253	-38.431	H
K293	177.384	58.312	32.557	119.862	7.383	-67.08	-41.186	H
V294	178.229	66.987	31.115	118.121	7.617	-65.324	-43.455	H
F295	179.04	58.901	37.849	117.423	8.799	-67.491	-22.581	H
K296	176.482	58.196	31.532	115.976	8.114	-73.387	-19.359	H
N297	172.627	54.423	41.163	117.794	7.558	-110.915	-13.057	L
M298	175.281	54.762	37.236	117.82	7.367	-128.05	148.831	L
S299	174.456	58.436	63.878	116.977	8.738	-69.844	157.465	L
K300	179.291	60.236	32.405	123.487	8.742	-57.669	-39.682	H
R301	178.34	58.384	29.716	117.395	8.604	-66.637	-38.452	H
A302	180.947	54.974	18.438	121.739	7.699	-65.247	-41.144	H
A303	179.108	55.395	18.672	122.011	8.789	-64.553	-41.058	H
E304	178.981	59.494	29.418	118.176	7.989	-64.255	-42.764	H
M305	178.024	58.821	33.187	117.12	7.867	-65.8	-42.568	H
M306	178.008	58.539	31.645	118.893	8.191	-63.802	-43.926	H
R307	179.221	60.577	29.76	119.691	8.461	-62.655	-42.883	H
D308	179.124	57.338	39.88	119.45	7.591	-66.191	-41.04	H
D309	179.975	57.664	40.074	122.705	8.541	-64.58	-40.37	H
I310	178.344	64.987	37.978	119.157	8.783	-65.08	-36.025	H
E311	177.494	58.796	29.216	120.564	7.851	-70.033	-20.033	H
A312	178.01	52.661	19.51	117.939	7.378	-87.792	-7.159	L
M313	173.633	54.938	33.403	120.538	7.415	-72.243	137.304	L
P314	not assigned	not assigned	not assigned	not assigned	-	-66.148	150.852	L
P315	176.162	63.645	31.929	not assigned	-	-60.521	142.434	L
V316	176.407	60.385	33.421	122.504	8.281	-93.005	133.288	L
R317	178.465	56.513	30.475	127.219	9.121	-70.591	140.554	L
V318	178.035	67.192	31.49	124.769	8.755	-55.289	-42.38	H
A319	180.82	55.08	18.43	120.139	8.763	-63.193	-35.074	H
D320	179.203	56.567	40.638	117.154	7.258	-70.563	-38.333	H
V321	177.987	67.353	31.565	124.057	7.953	-64.912	-43.191	H
E322	179.211	59.675	29.263	119.331	8.446	-64.39	-40.303	H
A323	180.299	55.156	18.162	120.088	7.692	-65.672	-40.755	H
A324	179.053	55.197	19.044	123.06	7.69	-66.768	-41.006	H
Q325	178.812	59.22	28.041	117.243	8.512	-64.39	-41.314	H
K326	179.601	60.133	32.435	117.54	8.03	-64.635	-41.167	H
E327	179.384	59.596	29.2	121.198	7.809	-65.224	-42.279	H
I328	177.756	66.325	37.241	119.221	8.007	-63.091	-42.535	H
L329	178.374	57.924	41.562	120.028	8.678	-65.158	-38.457	H
A330	181.306	55.409	17.748	121.807	8.089	-64.878	-39.445	H
I331	177.905	65.522	38.629	120.852	7.74	-65.921	-43.689	H
A332	179.153	55.145	17.55	121.881	8.574	-64.223	-37.27	H
R333	178.152	59.654	30.031	116.958	8.725	-63.931	-41.914	H
R334	180.052	59.689	29.549	119.973	7.653	-65.46	-42.073	H
M335	178.72	59.535	33.856	119.393	8.302	-65.023	-43.367	H
A336	182.136	54.901	17.799	124.621	8.83	-61.839	-40.467	H
D337	177.453	57.119	40.213	121.78	8.663	-66.251	-26.491	H
A338	177.759	52.185	19.304	119.235	7.479	-83.331	-5.619	L
G339	175.01	45.669	-	107.048	7.973	78.502	15.866	L
E340	175.046	56.645	31.208	117.218	8.21	-93.843	-11.874	L
L341	174.437	53.908	45.409	116.945	7.096	-132.987	139.332	E
M342	175.007	54.395	33.072	123.872	8.947	-105.787	122.38	E
L343	176.701	54.359	41.84	124.19	8.516	-82.796	137.654	E
S344	174.826	58.3	64.122	115.526	8.139	-82.838	155.079	L
G345	174.68	45.448	-	110.441	8.584	-175.301	173.041	L
G346	174.037	45.224	-	108.85	8.421	93.581	1.596	L
A347	177.624	52.726	19.331	123.655	8.327	-72.836	-19.306	L
D348	176.231	54.622	41.113	119.088	8.351	-72.792	-17.367	L
E349	175.952	56.797	30.367	120.498	8.191	-88.581	-6.85	L
F350	174.767	57.509	39.402	120.36	8.238	-86.071	136.833	L
L351	182.389	56.807	43.443	128.484	7.741	-	-	L

*1 ^{1}H, ^{13}C and ^{15}N chemical shifts are referenced indirectly against DSS.
*2 The backbone dihedral angles (phi and psi) for each residue are predicted from chemical shift data using TALOS-N [23].
*3 The secondary structure was predicted from TALOS-N [23].
H:α-helix; E: β-strand; L: coil